Supporting Information

Universal Non-destructive Interconnection Layer Engineering for Efficient and Stable Perovskite Tandem Photovoltaics

*Jiandong He, ‡[a,b,g] Jianan Wang, ‡[c] He Zhu, ‡[c] Ruihan Wu, ‡[b,g] Xuepeng Chen,[a] Dongni Li, [d] Youyu Jiang, [c] Keli Wang, [a,e] Changling Zhan, [a] Peng Gao, [a] Yabin Ma, [a] Rui Zhu, [a,h] Jing Li,[f] Chengbo Tian,[h] Zhanhua Wei,[h] Lei Meng, [b,g] Yinhua Zhou, [c] Wei Chen, [c] Yicheng Zhao, *[d] Zonghao Liu, *[c] Qing Zhao*[a,i]*

[a]State Key Lab for Mesoscopic Physics and Frontiers Science Center for Nano-optoelectronics, School of Physics, Peking University, Beijing, 100871, China.

[b]Beijing National Laboratory for Molecular Sciences, CAS Key Laboratory of Organic Solids, Institute of Chemistry, Chinese Academy of Sciences, Beijing, China.

[c]Wuhan National Laboratory for Optoelectronics and School of Optical and Electronic Information, Huazhong University of Science and Technology, Luoyu Road 1037, Wuhan 430074, Hubei, China.

[d]State Key Laboratory of Electronic Thin Films and Integrated Devices, School of Integrated Circuit Science and Engineering, University of Electronic Science and Technology of China, Chengdu 611731, China.

[e]Institute of Atomic and Molecular Physics, Sichuan University, Chengdu, 610065, China.

[f]Key Laboratory of Photochemical Conversion and Optoelectronic Materials, Technical Institute of Physics and Chemistry, Chinese Academy of Sciences, Beijing 100190, China.

[g]University of Chinese Academy of Sciences, Beijing, China.

[h]Institute of Luminescent Materials and Information Displays, College of Materials Science and Engineering, Huaqiao University, Xiamen 361021, China.

[i]Peking University Yangtze Delta Institute of Optoelectronics, Nantong, 226010, Jiangsu, China.

‡These authors contributed equally to this work.

*Corresponding author. Email: zhaoyicheng@uestc.edu.cn; liuzonghao@hust.edu.cn;

zhaoqing@pku.edu.cn.

Methods

Materials

Indium tin oxide (ITO) and fluorine-doped tin oxide (FTO) glass were purchased from SuZhou ShangYang Solar Technology. PM6 and BTP-eC9 were purchased from Solarmer Material. FAI and MAI were purchased from Greatcell Solar Materials. Nickel oxide nanocrystals (NiO_X) and 4PADCB were commercially available from Advanced Election Technology. C_{60}, $PC_{61}BM$ and BCP were purchased from Lumtec. [4-(3,6-Dimethyl-9H-carbazol-9-yl)butyl]phosphonic acid (Me-4PACz) was purchased from TCI. PbI_2 (super dry beads, 99.999%), CsI (super dry beads, 99.999%), $PbBr_2$ (super dry beads, 99.999%), tin(II) fluoride (SnF_2, 99%), and tin(II) iodide (SnI_2, beads, 99.99%, trace metals basis), Lead sulfocyanide [$Pb(SCN)_2$] (99.5%, trace metals basis), poly(ethyleneimine) solution (PEI, 50 wt% in H_2O), N,N-dimethylformamide (DMF, 99.8%), dimethyl sulfoxide (DMSO, 99.9%), chlorobenzene (99.9%), chloroform (99.8%), isopropanol (IPA; 99.7%), ethyl acetate (EA), anhydrous ethanol, 3,4-ethylenedioxythiophene (EDOT), $FeCl_3$ and Al_2O_3 dispersion (50 nm, 20 wt% in IPA) were purchased from Sigma-Aldrich. Glycine hydrochloride (GlyHCl) was purchased from Alfa Aesar. Poly(3,4-ethylenedioxythiophene):poly(styrene sulfonate) (PEDOT:PSS) aqueous solution (Al-4083), Lead chloride ($PbCl_2$), methylammonium chloride (MACl) ethylenediammonium diiodide ($EDAI_2$, 99.99%) and 1,3-propanediamine dihydriodide ($PDAI_2$, 99.99%) were purchased from Xi'an Yuri Solar Co., PDINN was purchased from Nanjing Zhiyan. Cyclohexane-1,4-diamine isomers were purchased from Shanghai Aladdin Biochemical Technology. Aquivion® PFSA (perfluorosulfonic acid) ionomer dispersion (D72-25BS, D79-25BS or D98-25BS) was purchased from Beijing Apslong Science and Technology. Tetrakis (dimethylamino) tin (IV) (99.9999%) for atomic layer deposited (ALD) SnO_2 was bought from Nanjing Ai Mou Yuan Scientific Equipment Co., Ltd. PDINN was purchased from Nanjing Zhiyan. Copper (99.999%), silver (99.999%) and gold (99.999%) were purchased from ZhongNuo Advanced Material (Beijing). Unless otherwise specified, all the chemicals and solvents were used without further purification.

Synthesis of PEDOT:F_A IPA dispersion

2 mL of Aquivion® PFSA (perfluorosulfonic acid) ionomer dispersion (25 wt% aqueous solution, 0.38 mmol) was mixed with 21 mg of EDOT (0.187 mmol) and 10 mL of H_2O. The mixture was sonicated for 20 minutes to form an emulsion, followed by stirring at room temperature for 2 hours. Then, 121 mg of $FeCl_3$ (0.75 mmol) was added, and the reaction was stirred for 6 hours. After completion, the resulting polymer dispersion was purified using a semipermeable membrane to remove residual oxidant and EDOT monomer, yielding a blue product. The resulting product was dispersed in IPA and sonicated using a horn probe sonic tip overnight to make dark blue PEDOT:F_A IPA dispersions.

Synthesis of *cis*-$CyDAI_2$

The cis-cyclohexane-1,4-diamine (1 mmol) and HI (2.2 mmol) were added to ethanol (with excess

HI to ensure a complete reaction) and stirred overnight at room temperature. On completion of the reaction, a large amount of diethyl ether was added as a precipitating solvent to obtain *cis*-CyDAI$_2$. The resulting precipitate was washed with diethyl ether and EA by centrifugation. The product was then dried for subsequent use.

Device fabrication

Single-junction 1.8 eV-WBG PSCs

The ITO substrates were sequentially cleaned using detergent, deionized water, acetone and ethanol consecutively, each by sonication for 15 min. The ITO glass substrates were dried with nitrogen flow and treatment with ozone generated by UV light for 15 min was done. NiO_x nanocrystal (10 mg mL^{-1} in H_2O) layers were first spin-coated on ITO substrates at 4000 rpm for 30 s in air and annealed on a 150 °C hotplates for 10 min, then the substrates were immediately transferred to the glovebox. first. Me-4PACz (0.5 mg mL^{-1}) dissolved in ethanol was spin coated on the ITO substrates at 3000 rpm for 30 s and then annealed at 100 °C for 10 min. The Al_2O_3 IPA dispersion solution (v/v, 1:150) was spin coated onto the HTL at 6000 rpm for 30 s and annealed at 100 °C for 5min. To prepare WBG perovskite precursor ($Cs_{0.2}FA_{0.8}Pb(I0_{.6}Br_{0.4})_3$) with a concentration of 1.5 M, CsI (0.3 M), FAI (1.2 M), PbI_2 (0.6 M) and $PbBr_2$ (0.9 M) were dissolved in 1 ml of mixed DMF/DMSO solvent (v/v, 3:1). It should be noted that 3 mol% of $MAPbCl_3$ were added to the perovskite precursor for device fabrication. The solutions were stirred overnight at room temperature, and no filtration was required before use. Then the perovskite solution was spin coated on the substrate at 4000 rpm for 30 s with an acceleration of 1000 rpm s^{-1}, during which 200 μL CB was dripped onto the center of film at 10 s before the end of spin-coating. The as-coated precursor films were subsequently annealed on a hotplate at 100 °C for 15 min. After cooling down, 80 μL of $PDAI_2$ (1 mg mL^{-1} in IPA) solution was spin coated onto the as-prepared perovskite films at 4000 rpm for 30 s with an acceleration of 4000 rpm s^{-1} and annealed at 100 °C for 5 min. 20-nm-thick C_{60} film was subsequently deposited on top by thermal evaporation at a rate of 0.2 A s^{-1}. Alternatively, we can use PCBM/PEI to replace C_{60}. A layer of $PC_{61}BM$ (20 mg mL^{-1} in CB, 1500 rpm, 30 s) was coated and annealed at 100 °C for 10 min. PEI solution (0.025 wt% diluted in IPA) was spin coated at 4000 rpm for 30 s (2000 rpm s^{-1} acceleration) without post-processing. 20 nm of ALD-SnO_2 was then deposited on top and followed by depositing 120 nm-Cu by thermal evaporation as the back electrode under a vacuum of 2×10^{-6} torr.

Single-junction NBG PSCs

Pre-patterned FTO glass substrates were sequentially cleaned using acetone and isopropanol. The substrates were then dried under a nitrogen flow and treated with UV-generated ozone for 15 min. PEDOT:PSS or PEDOT:F_A was spin-coated onto the FTO substrates at 6000 rpm for 30 s, followed by thermal annealing on a hotplate at 150 °C for 20 min in ambient air. After cooling, the substrates were immediately transferred into a nitrogen-filled glovebox. Subsequently, Al_2O_3 IPA dispersion solution (v/v, 1:150) was spin-coated onto the hole transport layer (HTL) at 6000 rpm for 30 s and annealed at 100 °C for 5 min. The perovskite precursor solution (2.0 M) was prepared by dissolving 1.2 mmol FAI, 0.6 mmol MAI, 0.2 mmol CsI, 1.0 mmol PbI_2, 1.0 mmol SnI_2, 0.1 mmol SnF_2,

0.04 mmol GuaSCN, and 0.04 mmol GlyHCl in a DMF/DMSO mixed solvent (volume ratio 3:1). The solution was stirred at 45 °C for 2 h and then filtered using a 0.22-μm PTFE membrane prior to use. The filtered precursor was deposited via a two-step spin-coating process: (1) 1000 rpm for 10 s at 200 rpm s^{-1} acceleration, and (2) 4000 rpm for 40 s at 1000 rpm s^{-1} acceleration. During the second step, 400 μL of CB was dropped onto the spinning substrate at 20 s before completion. The coated substrates were subsequently annealed at 100 °C for 10 min. Posttreatment was carried out by spin-coating 0.5 mg mL^{-1} $EDAI_2$ (dissolved in a 1:1 v/v mixture of IPA and toluene) at 4000 rpm for 30 s, followed by annealing at 100 °C for 5 min. Finally, 20 nm of C_{60}, 8 nm of BCP, and 120 nm of Cu were sequentially deposited on top of the perovskite layer by thermal evaporation under a vacuum of 2×10^{-6} torr.

All-perovskite TSCs

The WBG solar cells were prepared as described above. Following the deposition of ALD-SnO_2, the substrates were transferred back to the thermal evaporation system, where an ultrathin 1 nm layer of Au clusters was deposited onto the SnO_2 surface. Subsequently, a diluted PEDOT:PSS or PEDOT:F_A solution (volume ratio of 1:2 with IPA) was spin-coated onto the WBG subcell at 4000 rpm for 30 s, followed by annealing at 100 °C for 15 min under ambient conditions. The treated samples were then transferred into a nitrogen-filled glovebox. After the deposition of the Al_2O_3 dispersion, perovskite films, and $EDAI_2$ treatment, the substrates were transferred to the evaporation chamber. Under a vacuum of 2×10^{-6} torr, 20 nm of C_{60} was deposited. Then the ALD SnO_2 was prepared, then 100 nm Cu was deposited. Typically, an anti-reflective film was applied to the device surface to minimize light reflection and enhance optical absorption.

Single-junction 1.88 eV-WBG PSCs used for perovskite/organic TSCs

The pre-patterned FTO glass substrates were sequentially cleaned by sonication in detergent, deionized water, acetone, and isopropanol. After drying, the substrates were treated with UV–ozone for 15 min. A self-assembled monolayer (SAM) of 4PADCB (0.5 mg mL^{-1} in IPA) was then spin-coated onto the FTO substrates at 4000 rpm for 30 s, followed by annealing at 120 °C for 10 min. Once cooled to room temperature, Al_2O_3 IPA dispersion solution (v/v, 1:150) was dynamically spin-coated at 4000 rpm for 30 s and subsequently annealed at 100 °C for 5 min. The $FA_{0.7}MA_{0.2}Rb_{0.1}Pb(I_{0.5}Br_{0.5})_3$ perovskite precursor was prepared by adding 4 mol% $Pb(SCN)_2$ to a 1.5 M solution in DMF:DMSO (4:1 v/v). The mixture was stirred overnight and then filtered through a 0.22-μm PTFE membrane. A volume of 60 μL of the filtered perovskite solution was spin-coated onto the substrate at 4000 rpm. During the final 15 s of the spin-coating process, 200 μL of EA was swiftly dropped onto the center of the film. The resulting film was annealed at 100 °C for 15 min. Subsequently, a 0.3 mg mL^{-1} solution of *cis*-$CyDAI_2$ in IPA was spin-coated onto the perovskite film at 3000 rpm for 30 s, followed by annealing at 100 °C for 5 min. Finally, 25 nm of C_{60}, 8 nm of BCP, and 120 nm of Ag were sequentially deposited on top of the perovskite layer by thermal evaporation under a vacuum of 2×10^{-6} torr.

Single-junction NBG OSCs

The pre-patterned ITO glass substrates were cleaned and treated with UV–ozone following the same procedure used for the FTO glass substrates. A thin layer of PEDOT:PSS or PEDOT:F_A was spin-coated onto the ITO glass at 4000 rpm, followed by drying at 150 °C for 15 min in air. The PM6:BTP-eC9 blend (1:1.2 w/w) was dissolved in chloroform to a total concentration of 17.6 mg mL^{-1}, with 0.25% DIO added as a solvent additive. After stirring at 40 °C for 2 h, the active layer solution was deposited onto the PEDOT:PSS or PEDOT:F_A-coated substrates by spin-coating at 3000 rpm for 20 s, followed by thermal annealing at 100 °C for 5 min. Once cooled, a methanol solution of PDINN (1 mg mL^{-1}) was spin-coated on top of the active layer at 3000 rpm for 20 s. Finally, a 120 nm-thick Ag electrode was deposited via thermal evaporation under a vacuum of 2×10^{-6} torr.

Perovskite/organic TSCs

The monolithic perovskite–organic tandem solar cells were fabricated with the following device architecture: FTO/4PADCB/Al_2O_3/WBG perovskite/C_{60}/SnO_2/Au/ PEDOT:PSS or PEDOT:F_A/PM6:BTP-eC9/PDINN/Ag. The front sub-cell was prepared following the same procedure as that used for the single-junction perovskite solar cells. A 25 nm C_{60} layer was thermally deposited onto the perovskite active layer, followed by a 20 nm SnO_2 layer deposited via ALD. Subsequently, a 1 nm Au recombination layer was deposited by thermal evaporation at a rate of 0.1 Å s^{-1} under a base pressure of 2×10^{-6} torr. Subsequently, a diluted PEDOT:PSS or PEDOT:F_A solution (volume ratio of 1:2 with IPA) was spin-coated onto the WBG subcell at 4000 rpm for 30 s, followed by annealing at 100 °C for 15 min under ambient conditions. The treated samples were then transferred into a nitrogen-filled glovebox. The fabrication then continued following the same steps as the preparation of the single-junction organic solar cell. Finally, a 120 nm Ag electrode was deposited via thermal evaporation under high vacuum (2×10^{-6} torr).

Device characterizations

J-V curves were measured in a nitrogen atmosphere using an Agilent B2900 Series precision source/measure unit, with a scanning rate of 50 mV s^{-1} (voltage step of 10 mV and delay time of 200 ms), in both directions: from 1.21 V to -0.01 V (reverse scan) and from -0.01 V to 1.21 V (forward scan). The devices were illuminated by a Xenon lamp solar simulator (Solar IV-150A, Zolix) under AM 1.5G conditions (100 mW cm^{-2}), calibrated using a KG5-filtered Si reference cell from Newport. External quantum efficiency (EQE) and absorption spectra were measured in ambient air using a solar cell quantum efficiency/IPCE measurement system (Solar Cell Scan100, Zolix), also calibrated with a certified silicon solar cell. The scan interval was set to 1 nm, and no bias light was applied during the measurement. Additional EQE responses were obtained using a spectral response system (QE-R3-011, Enli Technology), where the light intensity at each wavelength was calibrated against a standard single-crystal Si photovoltaic cell. Electrochemical impedance spectroscopy (EIS) was performed under various bias voltages at an illumination intensity of 100 mW cm^{-2}. The AC amplitude was maintained at 70 mV, with frequencies ranging from 100 Hz to 10 MHz. Mott–Schottky analysis was conducted using the same AC amplitude

(70 mV), with frequency swept from 1 kHz to 100 kHz. The applied DC voltage varied from 0 V to 2 V in 35 steps.

Stability tests of solar cells

The operational stability of encapsulated perovskite solar cells (PSCs) was assessed under continuous AM 1.5G illumination (100 mW cm^{-2}) using a Class AAA multicolor LED solar simulator (Zhejiang Chint Electrics Co., Ltd). The maximum power point (MPP) was tracked in real time via a custom LabVIEW-based system employing the "perturb and observe" algorithm. The bias voltage was set to the initial MPP value determined from the *J–V* measurements. The current was continuously monitored at this fixed voltage using a Keithley 2450 source meter.

Film characterization

The crystal structure and phase composition were analyzed using an XPert Pro X-ray diffractometer (PANalytical, Netherlands) with Cu $K\alpha_1$ radiation (λ = 0.154 nm). Photoluminescence (PL) and time-resolved PL (TRPL) spectra were collected at room temperature using an FLS1000 spectrometer (Edinburgh Instruments). Ultraviolet-visible (UV-vis) absorption spectra were recorded on a SHIMADZU UV-2600 spectrophotometer. Surface and cross-sectional morphologies of the perovskite films and devices were observed using a scanning electron microscope (SEM, Quanta FEG 450) operated at an acceleration voltage of 10 kV. X-ray photoelectron spectroscopy (XPS) and ultraviolet photoelectron spectroscopy (UPS) data were obtained using a Kratos AXIS ULTRA DLD spectrometer. A non-monochromatic He I (21.22 eV) source served as the excitation source, and gold was used as the reference. A bias voltage of -9 V was applied during measurement. Absolute PL spectra of encapsulated samples were acquired using a hyperspectral imaging system (Photon etc. IMA), integrated with a microscope and a short-wave infrared (SWIR) camera. Samples were excited from the top perovskite surface using a 450 nm laser under 1-sun equivalent illumination (AM 1.5G, 100 mW cm^{-2}). Spectral data were processed using PHySpecV2 software to extract PL emission profiles. Quasi-Fermi level splitting (QFLS) was determined through quantitative analysis of the absolute PL spectra by fitting the generalized Planck equation, incorporating sub-bandgap absorption models and established fitting methodologies[1,2]. *In--situ* PL was recorded using a custom-built scanning confocal microscope equipped with a FLIMLABs 405 nm pulsed laser, a galvo scanner, and an IDQ time-correlated single photon counter.

Confocal laser scanning microscope

Confocal laser scanning microscopy (CLSM) characterization was performed using an inverted laser-scanning confocal microscope (FV3000, Olympus) equipped with a multi-line argon laser (458/488/514 nm) and solid-state lasers (405, 559, and 640 nm). Samples were excited through a high-numerical-aperture oil-immersion objective (UPlanSApo 60×, NA 1.35, Olympus), and the emitted fluorescence was spectrally separated using a diffraction-based spectral detector with an adjustable bandwidth range of 425-775 nm. Pixel dwell time was optimized between 2-8 µs to achieve a high signal-to-noise ratio while minimizing photobleaching. Sequential scanning was employed to eliminate cross-talk between fluorophores. Three-dimensional reconstructions were

generated from z-stacks acquired at 0.3 μm intervals, with optical sectioning thickness maintained below 0.8 μm using adjustable pinhole apertures (1-300 μm). All imaging was conducted under low laser power conditions (<5% of maximum output) to preserve sample viability and avoid saturation artifacts.

ToF-SIMS

ToF-SIMS measurements were carried out using a time-of-flight secondary ion mass spectrometer (ToF-SIMS 5, ION-TOF GmbH). Bi^+ ions were employed as the analysis source. All secondary-ion signals were collected from a 50 μm × 50 μm area. A 1 kV Ar^+ beam was used as the sputtering source to remove surface material during depth profiling, with the sputtering crater area set to 1000 μm × 1000 μm.

XPS depth profiling

XPS measurements were conducted using a ThermoFisher ESCALAB Xi+ system. A monochromatic Al Kα source (hv = 1486.6 eV) was used, with a pass energy of 20 eV. Samples were introduced into the XPS chamber via a vacuum transfer module to prevent air exposure. The binding energy scale of the spectra was calibrated against a cleaned gold (Au) reference. For XPS depth profiling, samples were sputtered layer-by-layer using a gas ion cluster beam (2000 cluster size) at 4 keV. The sampling point was located at the center of the sputtered crater (1 mm×1 mm). All characteristic elements present in the perovskite and hole transport layers served as fingerprints to distinguish the individual layers within the multilayer device architecture.

Transient photovoltage and transient photocurrent

Transient photovoltage (TPV) and transient photocurrent (TPC) measurements were performed using the all-in-one characterization platform PAIOS (Fluxim AG). For both TPC and TPV experiments, the light intensities were incrementally varied on a logarithmic scale at 10%, 17.8%, 31.6%, 56.2%, and 100% of 1-sun illumination.

AFM, KPFM and c-AFM

Surface morphology and electrical properties were characterized by using atomic force microscopy (AFM) systems under controlled environmental conditions. Surface roughness of the perovskite films was quantified using a Bruker Dimension Icon AFM operating in tapping mode (Nanoscope V controller) under ambient atmosphere. Work function measurements were conducted using Kelvin probe force microscopy (KPFM) on the same Bruker system within an argon-filled glovebox (<0.1 ppm O_2/H_2O), employing Pt-Ir-coated PPP-EFM probes (Bruker) in amplitude-modulated tapping mode to minimize surface disturbance. Local conductivity mapping was performed via conductive AFM (c-AFM) using a Bruker MFP-3D system integrated with a Nikon Eclipse inverted optical microscope. The customized piezo-stage allowed precise nanoscale current–voltage (I–V)

characterization under dark conditions. Conductive diamond-coated probes (Bruker DD-ACTA, spring constant ≈ 40 N/m) were used to ensure stable electrical contact. All AFM-based measurements were calibrated using standard reference samples: Bruker PG grating for topography and highly ordered pyrolytic graphite (HOPG) for electrical properties, ensuring high measurement fidelity.

Femtosecond transient absorption spectra

Femtosecond transient absorption (fs-TA) measurements were performed using a pump-probe spectrometer (Ultrafast Systems, Helios). An 800 nm laser beam with a pulse duration of 25 fs and a repetition rate of 1 kHz-generated by a regenerative-amplified Ti:sapphire laser (Legend Elite-1K-HE)-was used to generate the probe beam. The same Ti:sapphire laser also pumped a synchronized optical parametric amplifier (OPA, TOPAS), which produced a 380 nm pump beam for time-resolved excitation. After passing through an automated delay stage, the 800 nm beam was focused onto a sapphire crystal to generate a broadband white-light continuum (WLC) in the 460–810 nm range, which served as the probe. Both the pump and probe beams were then focused and spatially overlapped on the sample, with their temporal delay finely controlled by adjusting the optical path length via the programmed delay stage. Following sample interaction, the probe beam was collimated and directed into a fiber-coupled spectrometer for detection at 1 kHz. A synchronized chopper operating at 500 Hz modulated the pump pulses, enabling alternating acquisition of fs-TA spectra with and without pump excitation. The instrument response function (IRF) was approximately 120 fs. All measurements were performed at room temperature, and the data were processed using Surface Xplorer software.

Grazing-incidence wide-angle x-ray scattering

Grazing-incidence wide-angle X-ray scattering (GIWAXS) measurements were carried out at the BL14B1 beamline of the Shanghai Synchrotron Radiation Facility. The incident X-ray wavelength was 1.24 Å (10 keV). Diffraction patterns were recorded using a two-dimensional Mar225 detector. Instrument calibration was performed using a lanthanum hexaboride (LaB_6) standard sample.

Computational details

Numerical simulations were conducted using COMSOL Multiphysics 6.2 to investigate water infiltration and solute transport within a multilayered porous structure composed of SnO_2 and C_{60} layers[3]. To accurately model water transport in such nanostructured multilayer architectures, a coupled physics framework was adopted, integrating Darcy's Law for porous media flow with the Transport of Diluted Species in Porous Media module[4]. This approach is well-suited for thin-film systems with nanometric thicknesses, where water movement is primarily driven by slow, pressure-induced flow and concentration gradients across heterogeneous interfaces. The computational domain was constructed in two dimensions, with SnO_2 layer thicknesses parameterized at 20 nm and 30 nm. The aqueous phase and nanoscopic Au islands were modeled as boundary conditions rather than computational subdomains to better emulate interface-dominated transport behavior at

the nanoscale. This coupled approach enabled the simultaneous resolution of flow and diffusion processes, using the following governing equations[5,6]:

Darcy's Law for flow:

Darcy's Law describes incompressible, laminar flow in porous media and is applicable to systems with low Reynolds numbers and permeability, such as ALD-deposited SnO_2. It provides a computationally efficient means to evaluate water flux driven by pressure gradients, without resorting to full Navier–Stokes formulations[7]:

$$\rho\frac{\partial\epsilon}{\partial t} + \nabla \cdot (\rho u) = 0,$$

$$u = -\frac{k}{\mu}(\nabla + \rho g)$$

Transport of diluted species:

This module accounts for solute diffusion and advection influenced by the Darcy velocity field, enabling simulation of water concentration fronts and the interaction between molecular diffusion and convective flow across the oxide-organic interfaces:

$$\frac{\partial c}{\partial t} + \nabla \cdot (-D + cu) = 0$$

Due to the nanometric scale of the SnO_2 layer, the standard Subsurface Flow Module-typically used for bulk groundwater modeling-was not employed. Instead, the Transport of Diluted Species in Porous Media interface was selected for its ability to resolve coupled advection–diffusion dynamics in low-permeability nanostructures.

Boundary and initial conditions were defined based on experimentally relevant fluid exposure scenarios. Mesh refinement was implemented to enhance numerical precision, particularly at the SnO_2/C_{60} interface where sharp concentration gradients occurred. Parametric sweeps were conducted to systematically examine time-resolved concentration and infiltration profiles across SnO_2 layers of varying thickness.

Supplementary Note 1: Procedure for ICL removal

To systematically evaluate the degradation effects induced by aqueous PEDOT:PSS on WBG perovskite sub-cells, we established a reproducible protocol to isolate the underlying perovskite absorber after full device fabrication. As illustrated in **Fig. 1** and **Fig. S1**, the procedure begins with the complete soaking of PEDOT:PSS-based WBG front cells in CB at room temperature for weakening the adhesion between the ICL and underlying SnO_2 interface.

Following solvent processing, residual PEDOT and SnO_2/Au interlayers were mechanically delaminated using adhesive tape. The exposed surface was then rinsed and gently dried under nitrogen flow to yield a pristine and naked WBG perovskite film.

We note that simply rinsing the device in CB five times was insufficient to fully expose the WBG perovskite layer. In such cases, residual SnO_2/Au and PEDOT:PSS fragments remained strongly adhered to the perovskite surface (**Fig. S2a**), which prevented direct access for subsequent characterization. In contrast, immersing the samples in CB overnight allowed the solvent to gradually penetrate and weaken the interfacial adhesion within the ICL stack. This extended soaking step enabled complete removal of the SnO_2/Au/PEDOT:PSS layers without damaging the underlying WBG perovskite, resulting in a uniformly exposed and pristine perovskite film (**Fig. S2d**). This optimized protocol ensured reproducible isolation of the WBG absorber for accurate evaluation of HTL-induced degradation. FTIR and XPS results (Fig. S2e,f) reveal that for the control WBG perovskite and overnight soaking ICL removal WBG perovskite films, the FTIR and XPS survey spectra is almost identical. Regarding the sensitivity of FTIR and XPS analysis, we would like to highlight that top layers with ICL can be completely washed using overnight soaking ICL removal method. On the contrary, there is a clearly visible signals with residual Sn and Au for 5 times CB rinsing sample in the XPS spectra. Regarding the FTIR results, there is a clearly visible signals in ~1250 cm-1 for 5 times CB rinsing sample, which might be the residual C-O-C vibrational peak of PEDOT:PSS, indicating that simply rinsing the device in CB five times was insufficient to fully expose the WBG perovskite layer, while the developed overnight soaking method can effectively fully remove the top layers. The XPS and FTIR results reveal that overnight soaking ICL removal is an effective method to completely wash the top ICL layers compared to only 5 times rinsing in CB solution.

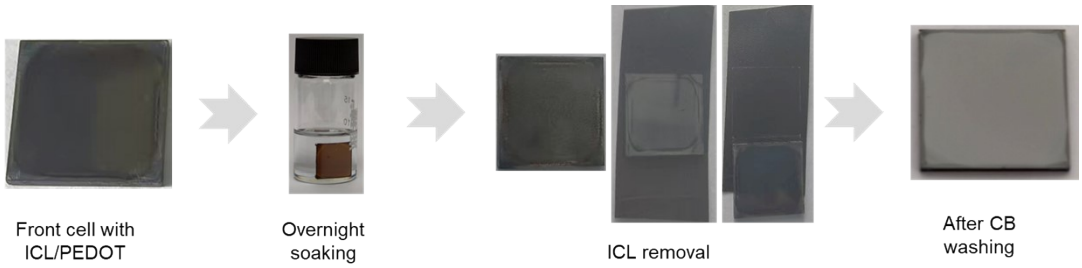

Fig. S1. Experimental photos for exposing the underneath WBG perovskite film.

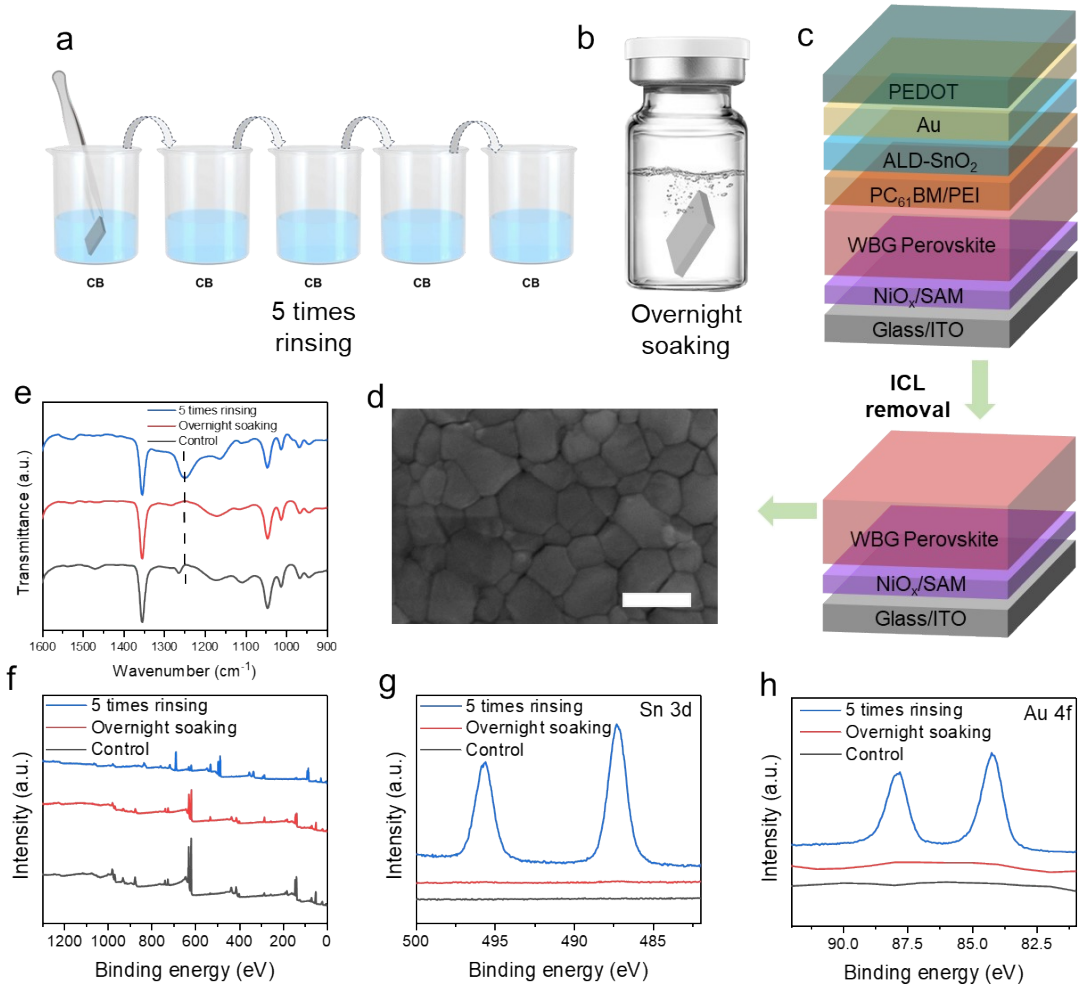

Fig. S2. (a) Schematic illustration for the WBG front cell rinsing. (b) Schematic illustration for the WBG front cell soaking. (c) Structural schematic diagram of the WBG front cell before and after ICL removal. (d) SEM image of the obtained WBG film. Scale bar, 500 nm. (e) FTIR peaks of the control WBG perovskite, 5 times rinsing and overnight soaking ICL removal WBG perovskite films on ITO substrates. (f) X-ray photoelectron spectroscopy (XPS) survey spectra of the control WBG perovskite, 5 times rinsing and overnight soaking ICL removal WBG perovskite films on ITO substrates. (g,h) XPS core-level spectra for Sn 3d (g) and Au 4f (h) identified in the survey scan.

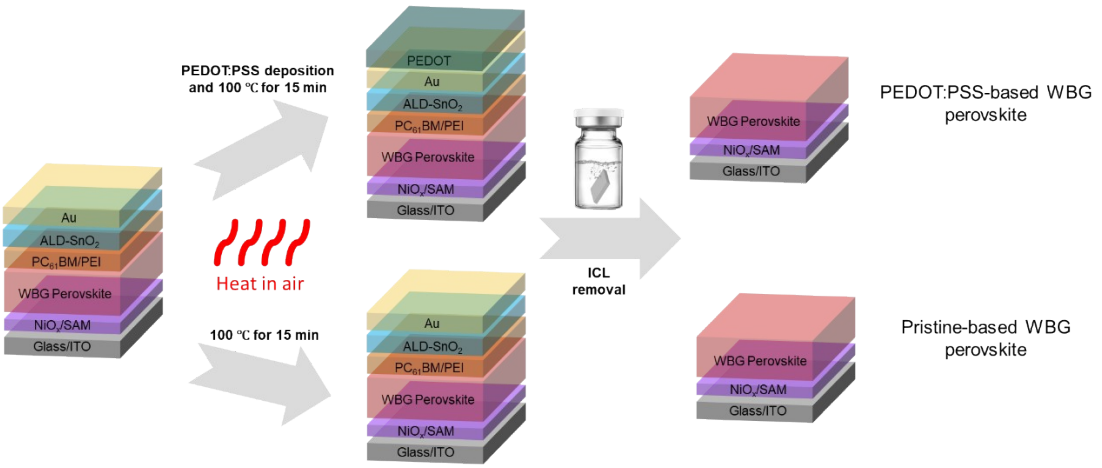

Fig. S3. Schematic illustration of ICL removal for PEDOT:PSS-based and Pristine-based (without PEDOT:PSS deposition) WBG perovskite process.

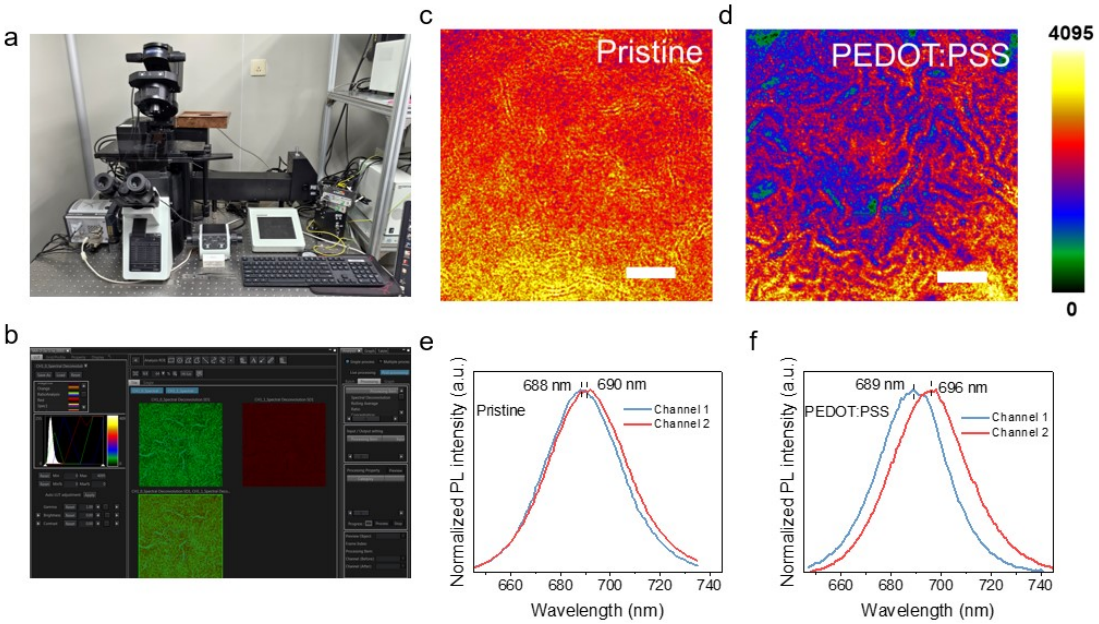

Fig. S4. (a) Photograph of CLSM experimental setup. (b) Software interface for the extraction of different wavelength channels in CLSM. PL mapping of the pristine (c) and PEDOT:PSS-based (d) WBG surface after ICL/HTL removal through CLSM. Scar bar, 10 μm. Corresponding PL spectra of pristine (e) and PEDOT:PSS-based (f) WBG perovskite film.

Supplementary Note 2: The reconstructed WBG perovskite devices

To unambiguously assess the effects of water-based HTLs on WBG perovskite stability, we designed and compared two distinct categories of WBG perovskite solar cells.

The **pristine-based reconstructed** devices were WBG PSCs followed by ICL deposition without HTL deposition. Then the above ICL was removed and the top contact (C_{60}/BCP/Cu) was re-deposited in sequence on the now-exposed WBG surface. These pristine devices represent the baseline performance of the WBG sub-cell without external HTL processing influences.

The second categories were **reconstructed devices**, designed to simulate the critical tandem fabrication step in which the WBG sub-cell is exposed to PEDOT:PSS HTLs via an ICL interface. In these configurations, we first deposited the full ICL/HTL stack onto the WBG perovskite, mimicking tandem integration. The stack was then mechanically removed, and the top contact (C_{60}/BCP/Cu) was re-deposited in sequence on the now-exposed WBG surface, as outlined in **Fig. S5**. This reconstruction strategy isolates the irreversible effects of HTL exposure—such as moisture erosion, interfacial reactions, or defect formation—on the buried perovskite interface.

Device reconstruction was applied consistently across all variants: C_{60}, BCP, and thermally evaporated Cu electrodes were deposited onto either previously HTL-exposed or unprocessed WBG films. This ensured uniformity in top-contact structure and enabled a direct, comparative evaluation of interface degradation induced by different HTL chemistries.

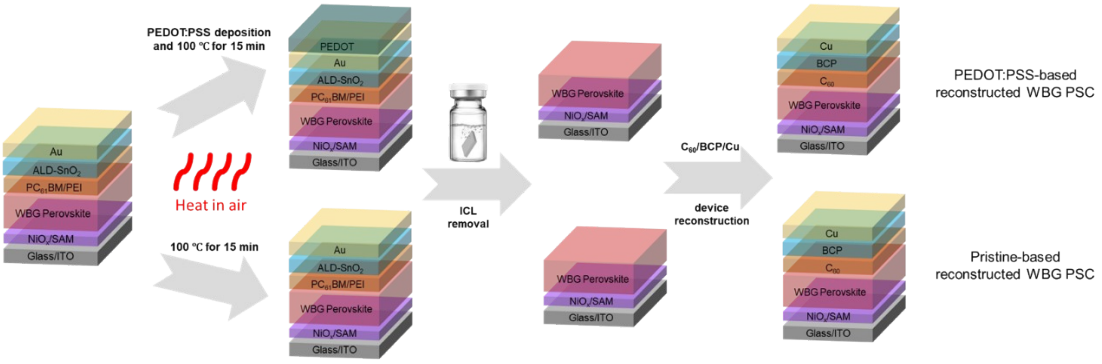

Fig. S5. Schematic illustration of PEDOT:PSS-based and Pristine-based (without PEDOT:PSS deposition) WBG PSCs reconstruction process.

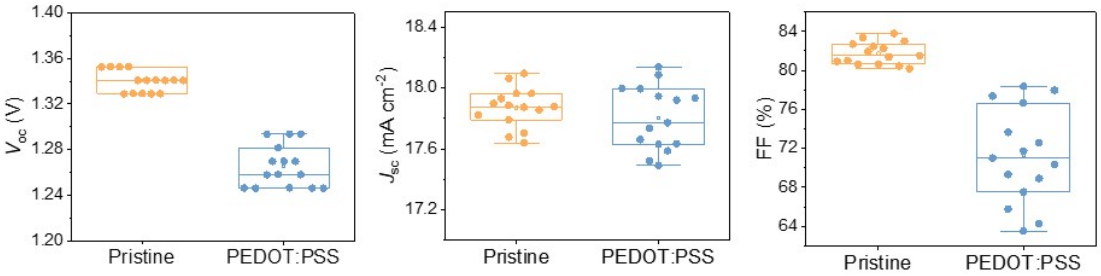

Fig. S6. Comparison of V_{oc}, J_{sc} and FF between Pristine and PEDOT:PSS-based WBG solar cells after ICL removal (15 devices for each type). The box lines indicate the standard deviation and the center represents the mean value.

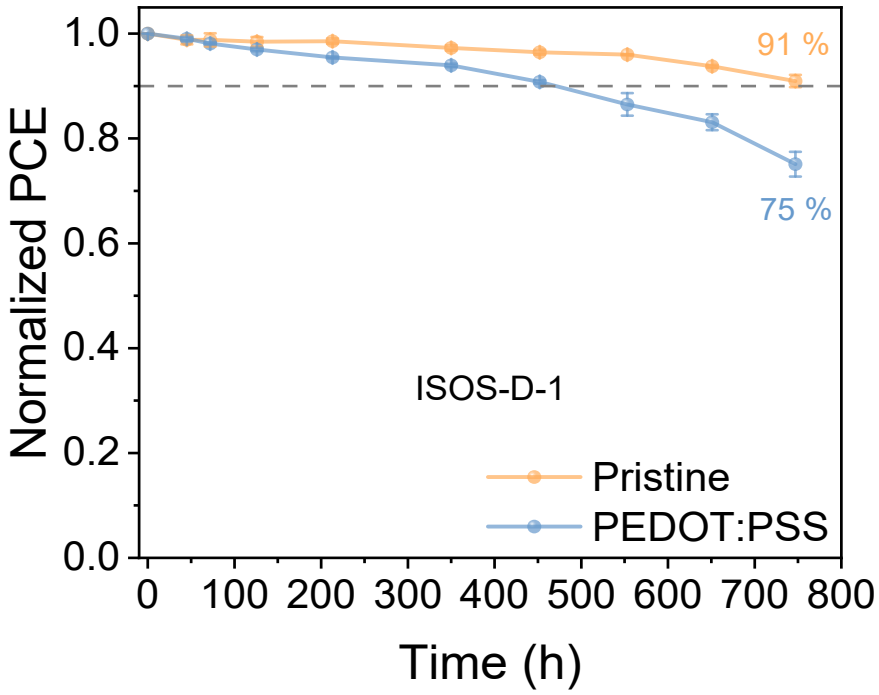

Fig. S7. Normalized PCE of unencapsulated devices aged under dark conditions in N_2 following the ISOS-D-1 protocol. Three devices for each type, error bars denote standard deviation.

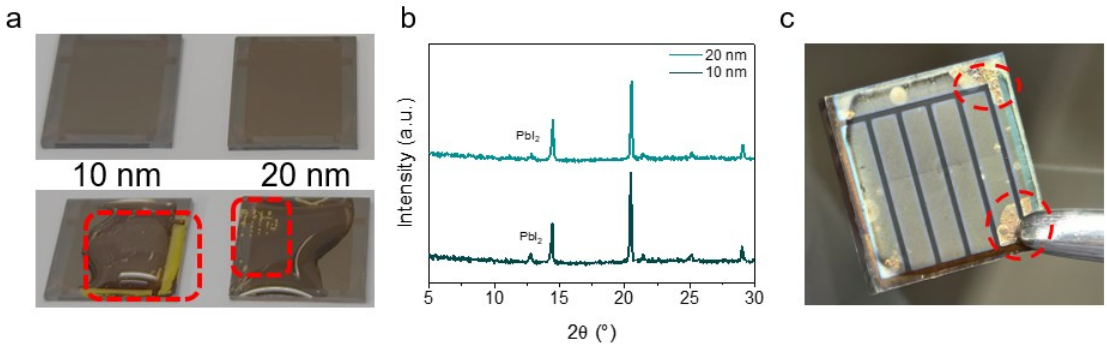

Fig. S8. (a) WBG perovskite/C_{60}/ALD-SnO_2/Au films with different SnO_2 thicknesses (10 and 20 nm) and corresponding water drop damage experiments after ~6 minutes. (b) XRD of WBG perovskite/C_{60}/ALD-SnO_2/Au films with different SnO_2 thicknesses (10 and 20 nm) after water drop damage experiments. (c) Photo of the PEDOT:PSS water damage to the WBG perovskite when using IZO with mask sputtering by replacing 1nm-Au with 100 nm-IZO.

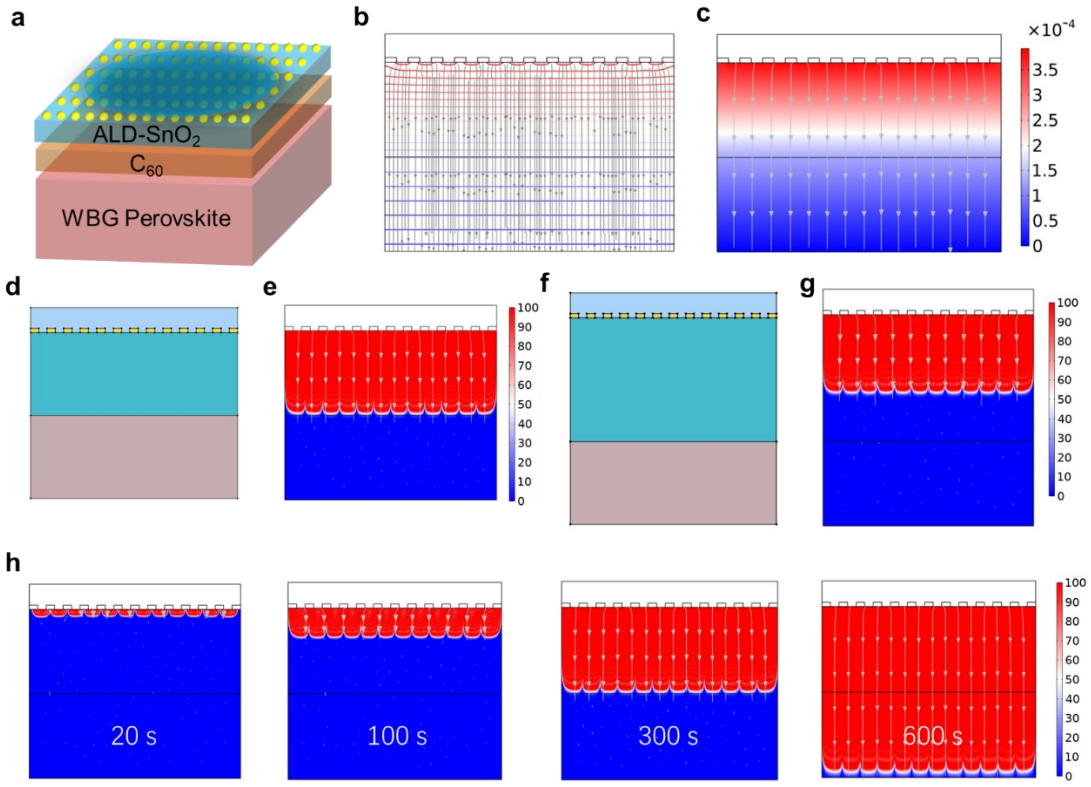

Fig. S9. (a) Mechanism of moisture erosion in the WBG perovskite front cell. A uniform circular array underneath water droplets demonstrates the tendency of 1-nm Au nanoparticles to form large and irregular Au islands on the SnO_2 surface. (b) COMSOL-simulated streamline network along the *z* direction (20 nm SnO_2) during moisture erosion at scaled time of 300 s. (c) COMSOL-simulated contour of pressure along the *z* direction (20 nm SnO_2) during moisture erosion at scaled time of 300 s. (d) COMSOL-simulated geometry along the *z* direction (20 nm SnO_2) during moisture erosion at scaled time of 300 s. (e) COMSOL-simulated contour of concentration along the *z* direction (20 nm SnO_2) during moisture erosion at scaled time of 300 s. (f) COMSOL-simulated geometry along the *z* direction (30 nm SnO_2) during moisture erosion at scaled time of 300 s. (g) COMSOL-simulated contour of concentration along the *z* direction (30 nm SnO_2) during moisture erosion at scaled time of 300 s. (h) The time evolution of COMSOL-simulated contour of concentration along the *z* direction (20 nm SnO_2) during moisture erosion.

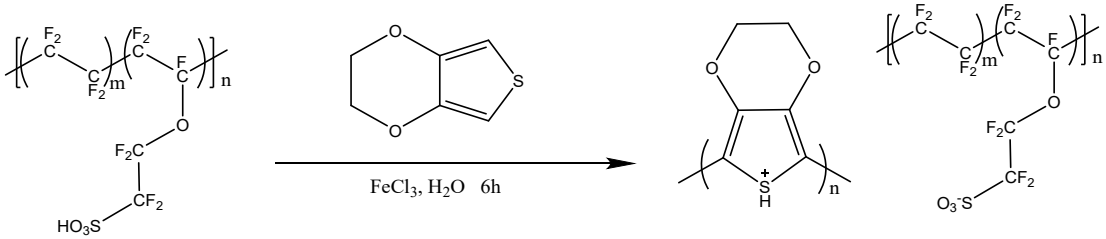

Fig. S10. Synthesis route of PEDOT:F_A.

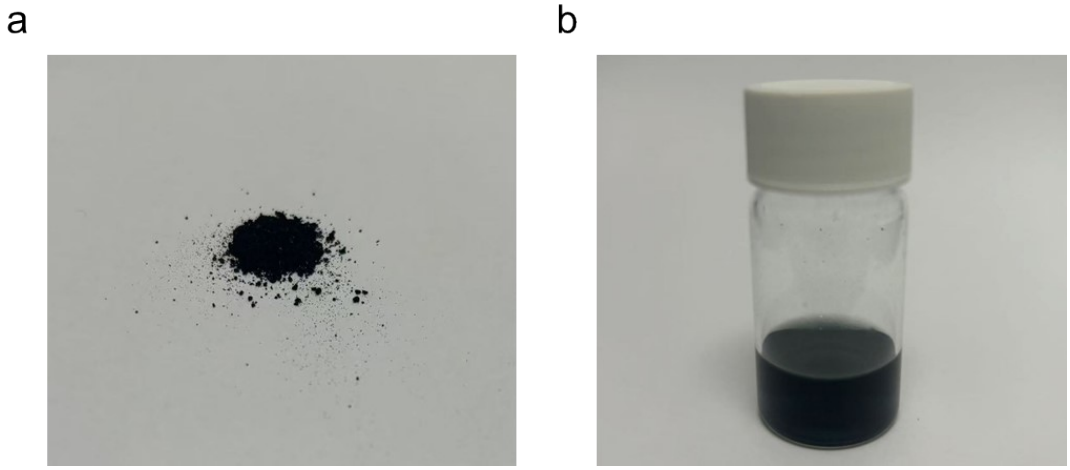

Fig. S11. (a) The powder of PEDOT:F_A after centrifugation and drying. (b) Solution processability of PEDOT:F_A in IPA.

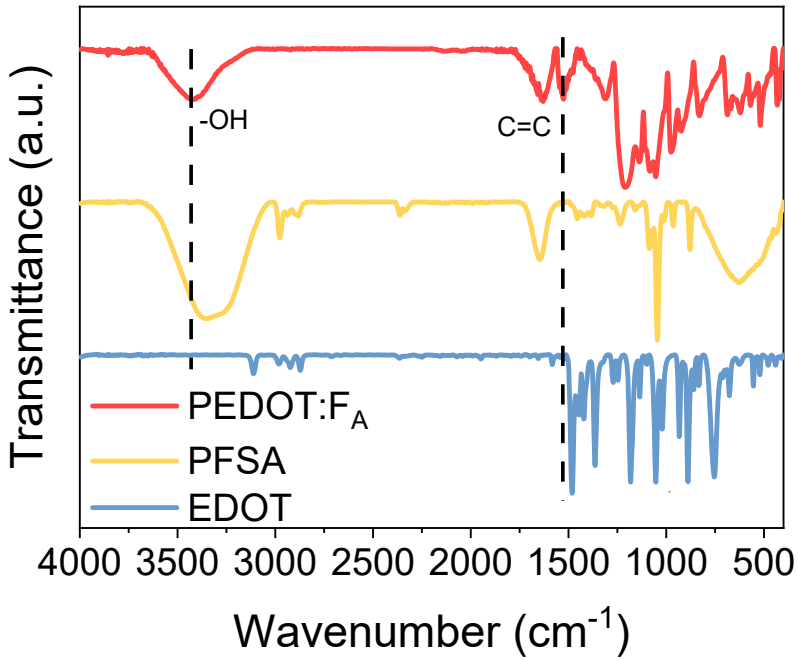

Fig. S12. FTIR peaks of 3,4-ethylenedioxythiophene (EDOT), Aquivion® PFSA, and PEDOT:F_A. The shifting peaks of -OH at ~3350 cm^{-1} to the higher wavenumber of ~3435 cm^{-1} for the PEDOT:F_A compound indicate stronger bonding due to oxidative polymerization. The ~1525 cm^{-1} new peak could correspond to the C=C stretching vibration of the conjugated thiophene ring and the polarization of the conjugated chain caused by PEDOT doped by the sulfonic acid groups (-SO_3H) in PFSA.

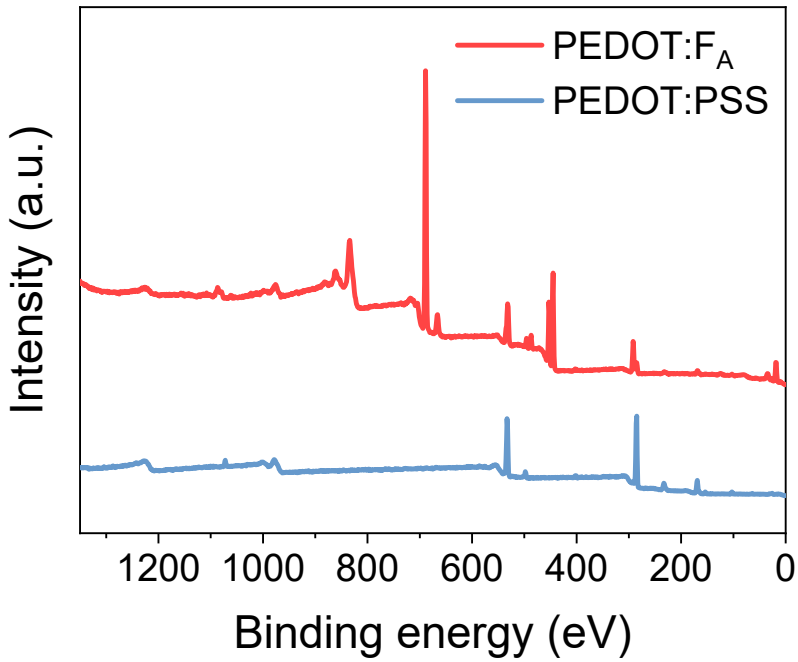

Fig. S13. XPS survey spectra of PEDOT:PSS and PEDOT:F_A films on ITO substrates, **Table S3** provides the specific percentages of each element.

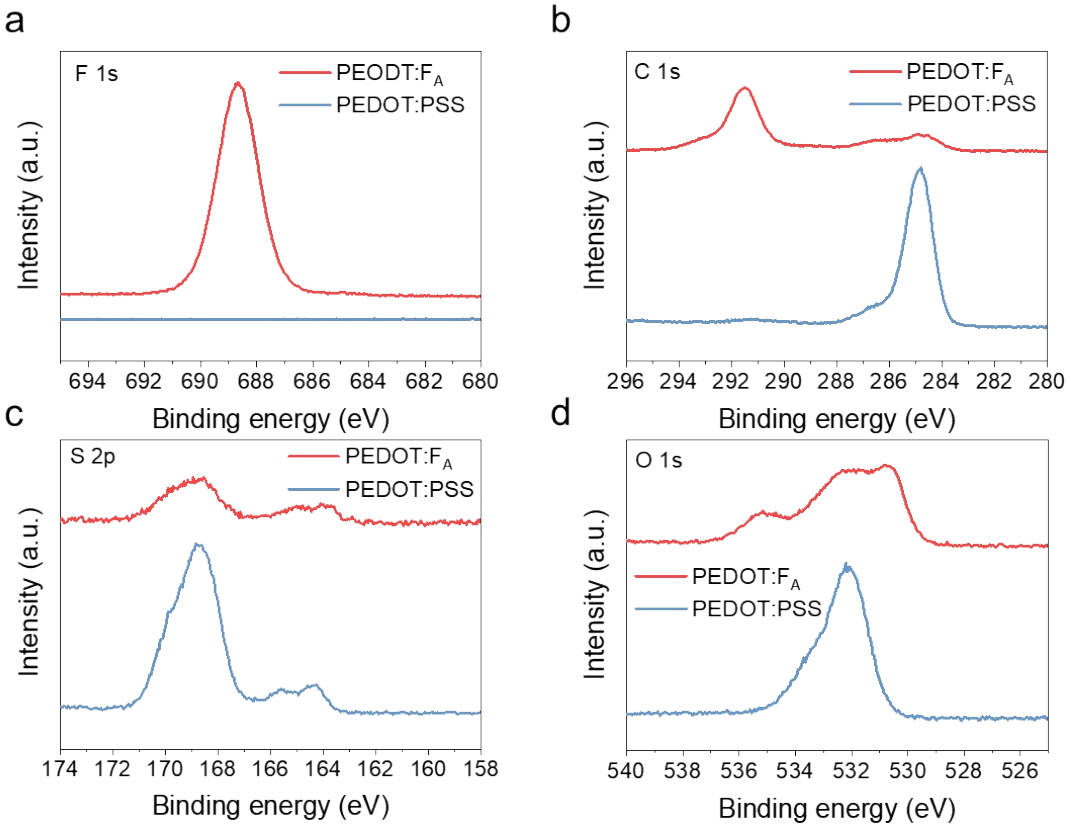

Fig. S14. High-resolution XPS core-level spectra for F 1s (a), C 1s (b), S 2p (c) and O 1s (d) identified in the survey scan.

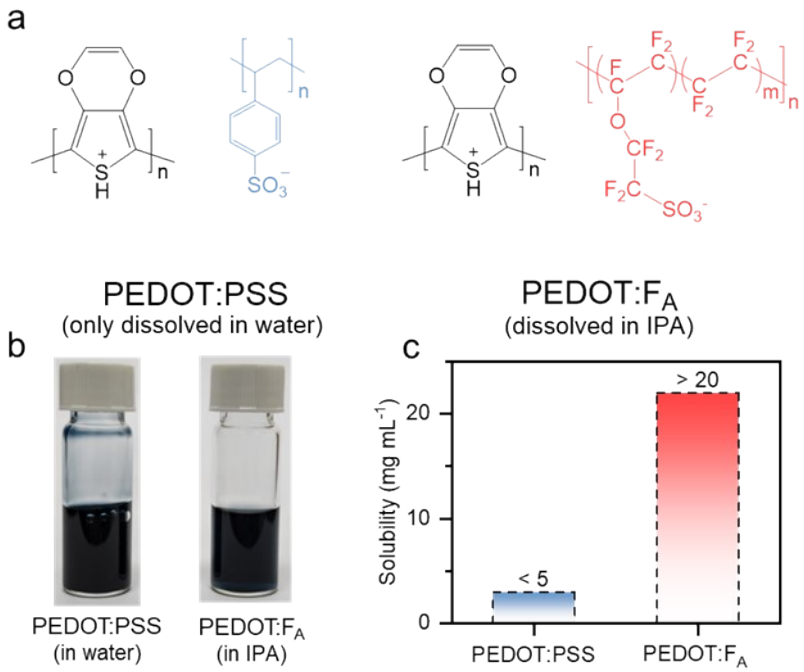

Fig. S15. (a) Chemical structures of PEDOT:PSS and PEDOT:F_A, PEDOT:PSS can only be dissolved in water, while PEDOT:F_A can be dissolved in IPA. (b) Photos of PEDOT:PSS water solution and PEDOT:F_A IPA solution. (c) Solubility of PEDOT:PSS and PEDOT:F_A in IPA.

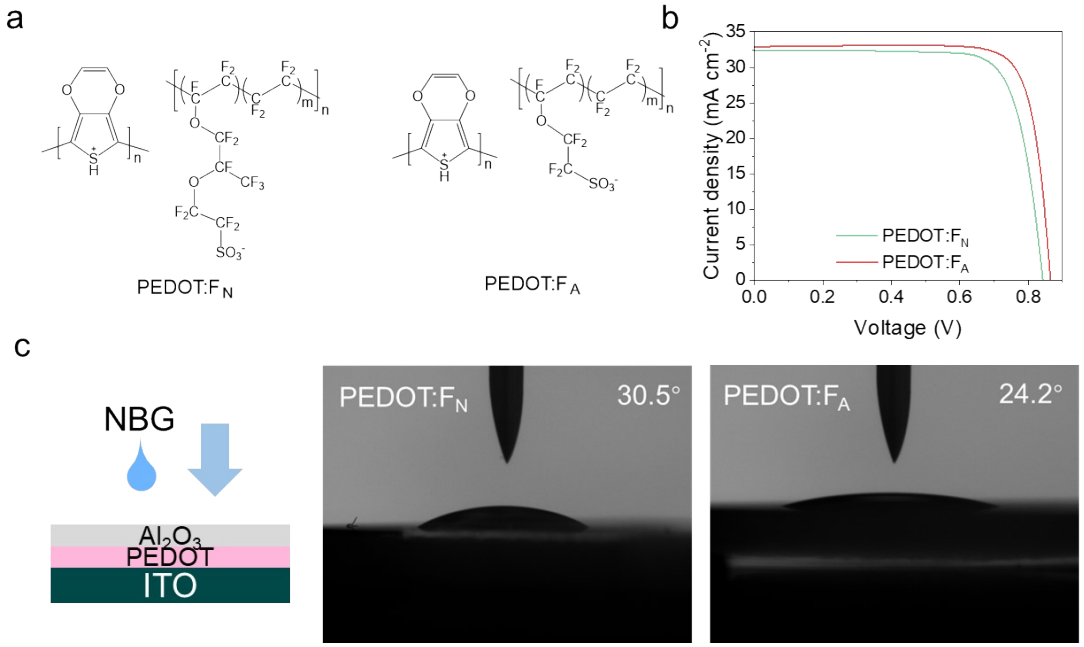

Fig. S16. (a) Chemical structure of PEDOT:F_N and PEDOT:F_A. IPA-dispersed PEDOT:F_N solution was synthesized based on the procedure reported by Jiang and co-workers[8]. (b) *J-V* curves of the PEDOT:F_N and PEDOT:F_A-based NBG devices. (c) Contact angle results of NBG perovskite solution on ITO/PEDOT/Al_2O_3 substrates, PEDOT donates PEDOT:F_N or PEDOT:F_A.

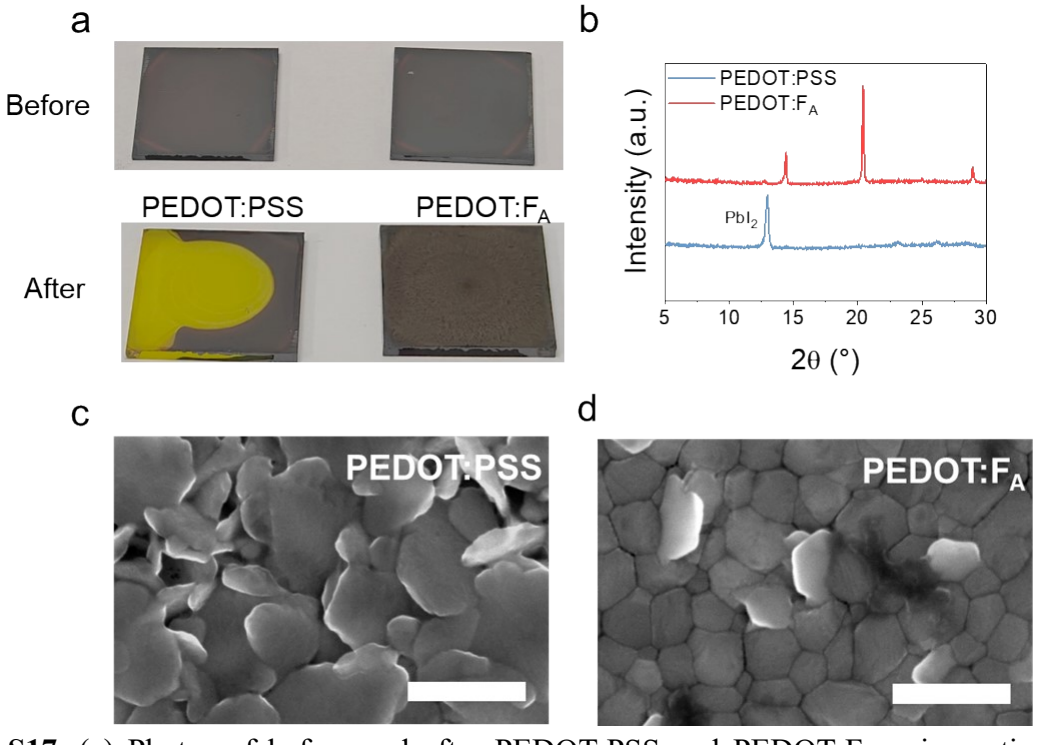

Fig. S17. (a) Photos of before and after PEDOT:PSS and PEDOT:F_A spin-coating directly on the top of the WBG perovskite films. (b) XRD of PEDOT:PSS or PEDOT:F_A spin-coated WBG perovskite films. The corresponding SEM images of the PEDOT:PSS (c) or PEDOT:F_A (d) spin-coated WBG perovskite films.

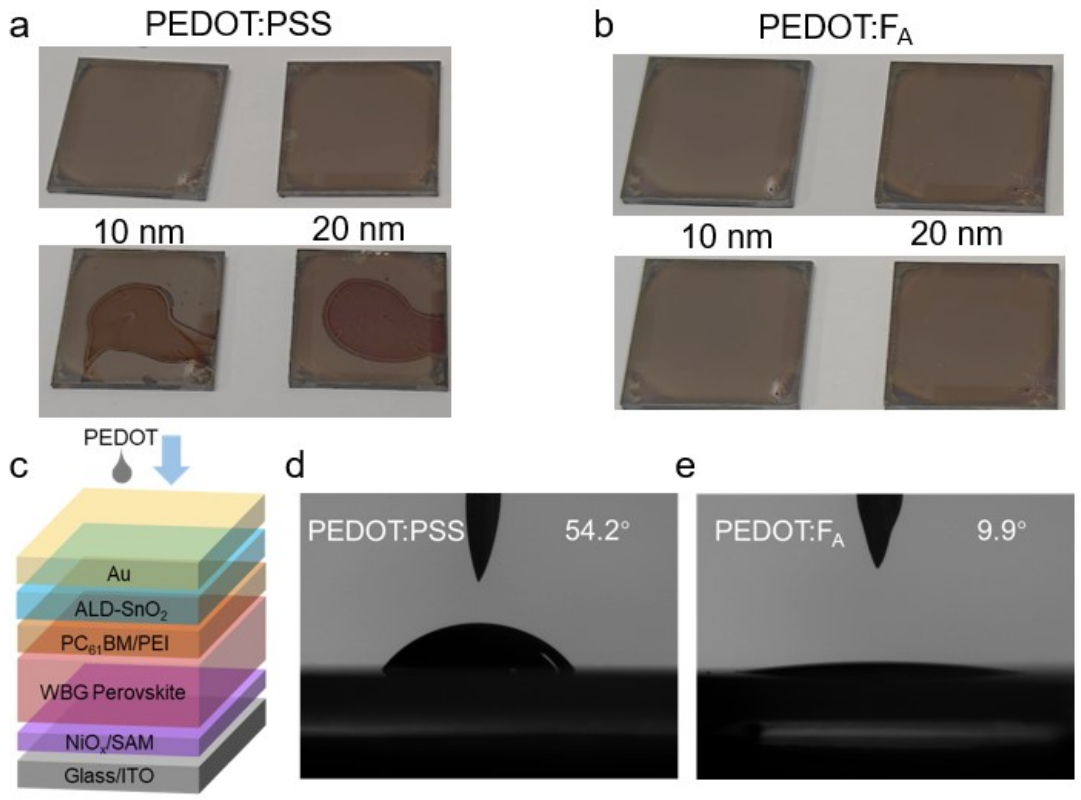

Fig. S18. Wettability Test of PEDOT:PSS and PEDOT:F_A on WBG perovskite/$PC_{61}BM$/PEI/ALD-SnO_2/Au films. (a,b) Photos of PEDOT:PSS (a) and PEDOT:F_A (b) dropped on WBG perovskite/$PC_{61}BM$/PEI/ALD-SnO_2/Au films. (c) Structure diagram of WBG perovskite/$PC_{61}BM$/PEI/ALD-SnO_2/Au dropped with PEODT:PSS or PEDOT:F_A. Contact angle results of PEDOT:PSS (d) and PEDOT:F_A (e) solution on WBG perovskite/$PC_{61}BM$/PEI/ALD-SnO_2/Au films.

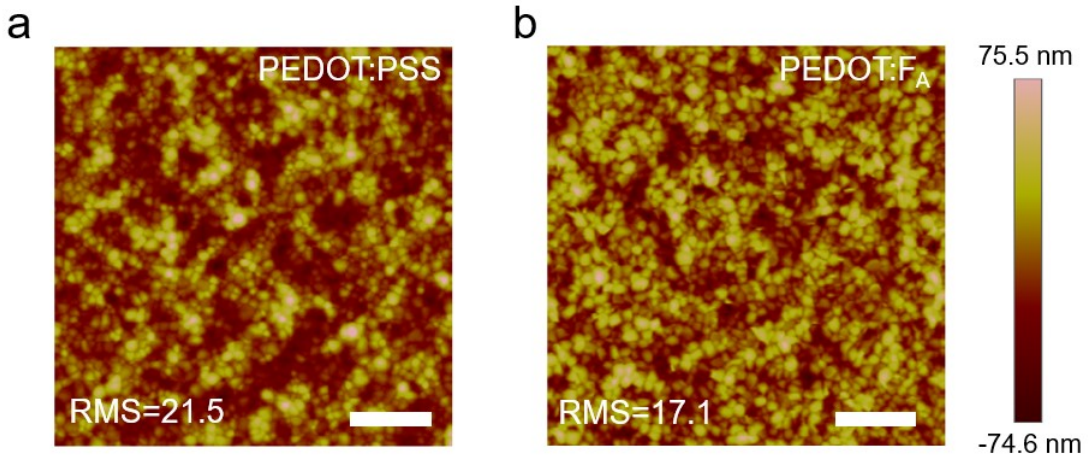

Fig. S19. Atomic force microscopy (AFM) images of PEDOT:PSS (a) and PEDOT:F_A (b) based WBG perovskite films after ICL removal. Scale bar, 2 μm

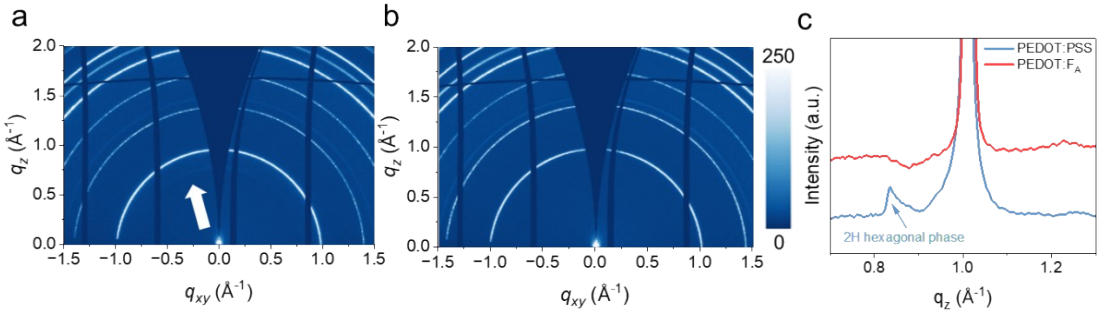

Fig. S20. GIWAXS images of WBG perovskite films prepared after PEDOT:PSS (a) or PEDOT:F_A (b) HTL spin-coating onto the front cells and ICL removal. (c) The zoom-in of radially integrated intensities of GIWAXS patterns fabricated using different PEDOT.

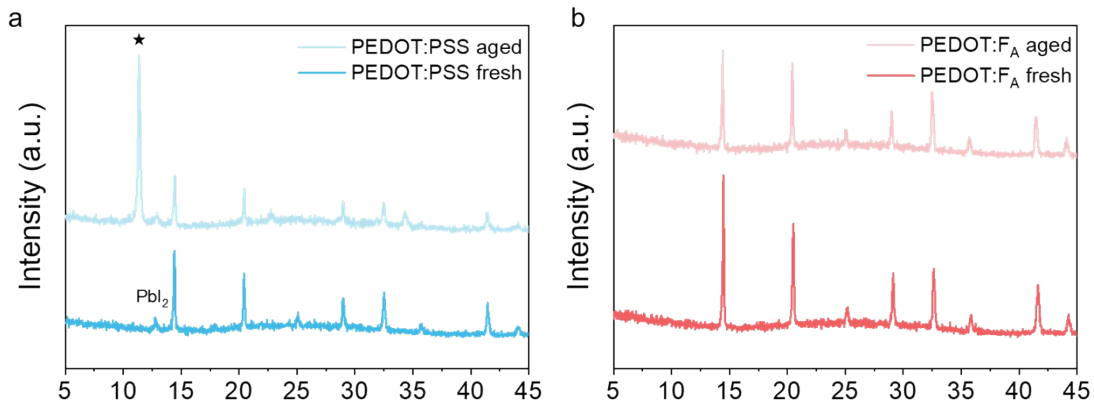

Fig. S21. XRD patterns of PEDOT:PSS (a) and PEDOT:F_A (b) prepared WBG perovskite films after ICL removal before and after 10-day aging in N_2 conditions (25 °C, dark storage, unencapsulated).

The additional peak marked with ★ in (a) corresponds to the 2H hexagonal phase, which emerges after aging in PEDOT:PSS-based films, indicating significant structural degradation. In contrast, no such phase is observed in PEDOT:F_A-based samples, underscoring their superior phase stability.

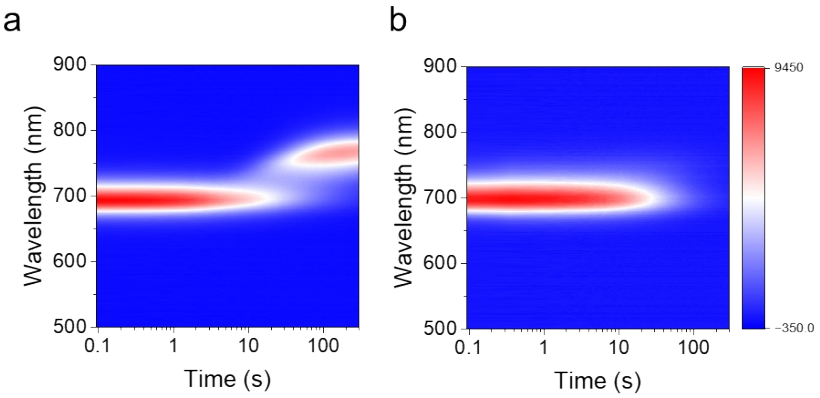

Fig. S22. In situ PL measurements with varying time of the PEODT:PSS (a) and PEDOT:F_A (b) based and ICL removed WBG perovskite films.

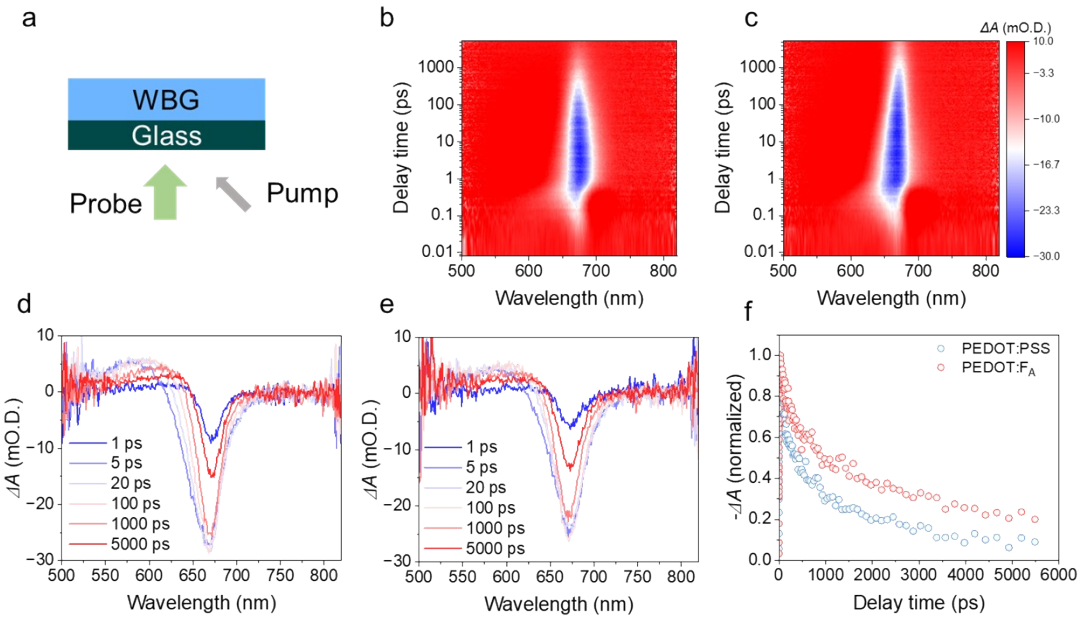

Fig. S23. (a) Setup of femto-second transient absorption (fs-TA) spectra with 405-nm pump light, pumped from the Glass side. fs-TA spectra patterns of PEDOT:PSS (b) and PEDOT:F_A (c) based WBG perovskite films after ICL removal. Time-dependent transient fs-TA spectra of PEDOT:PSS (d) and PEDOT:F_A (e) based WBG perovskite films. (f) The corresponding transient absorption change (measured in optical density) over a timescale of 6000 ps.

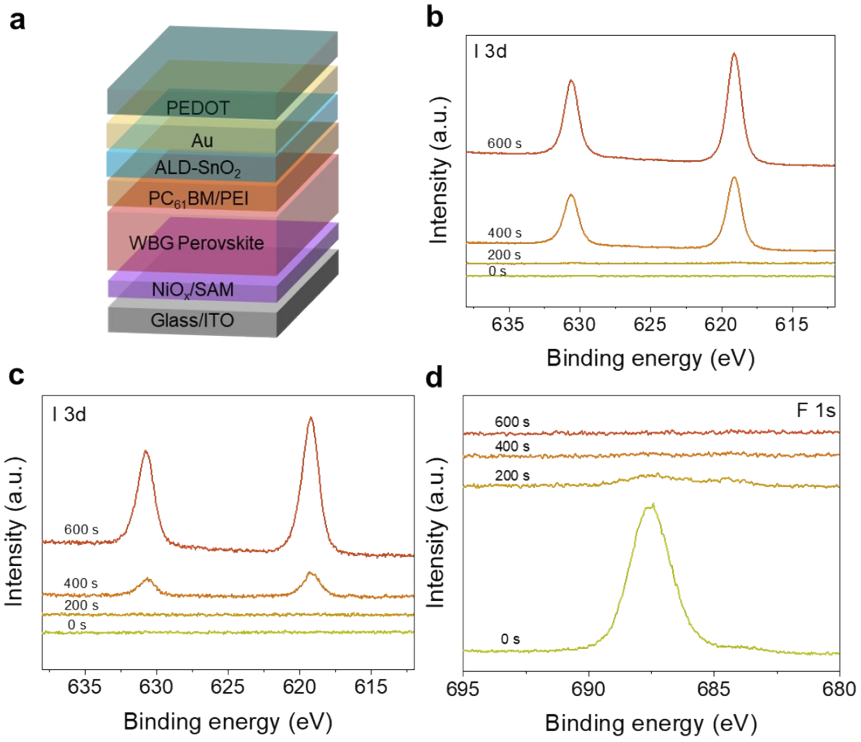

Fig. S24. (a) Structural schematic diagram of XPS depth profiling detected ITO/NiO_x/SAM/WBG/$PC_{61}BM$/PEI/SnO_2/Au/PEDOT front cells. Depth profiling proceeds from the top surface down through the device stack, revealing buried interfaces sequentially. XPS depth profiling of the PEDOT:PSS sample of (b) I 3d and the PEDOT:F_A sample of (c) I 3d and (d) F 1s detected at the top of the WBG front cells.

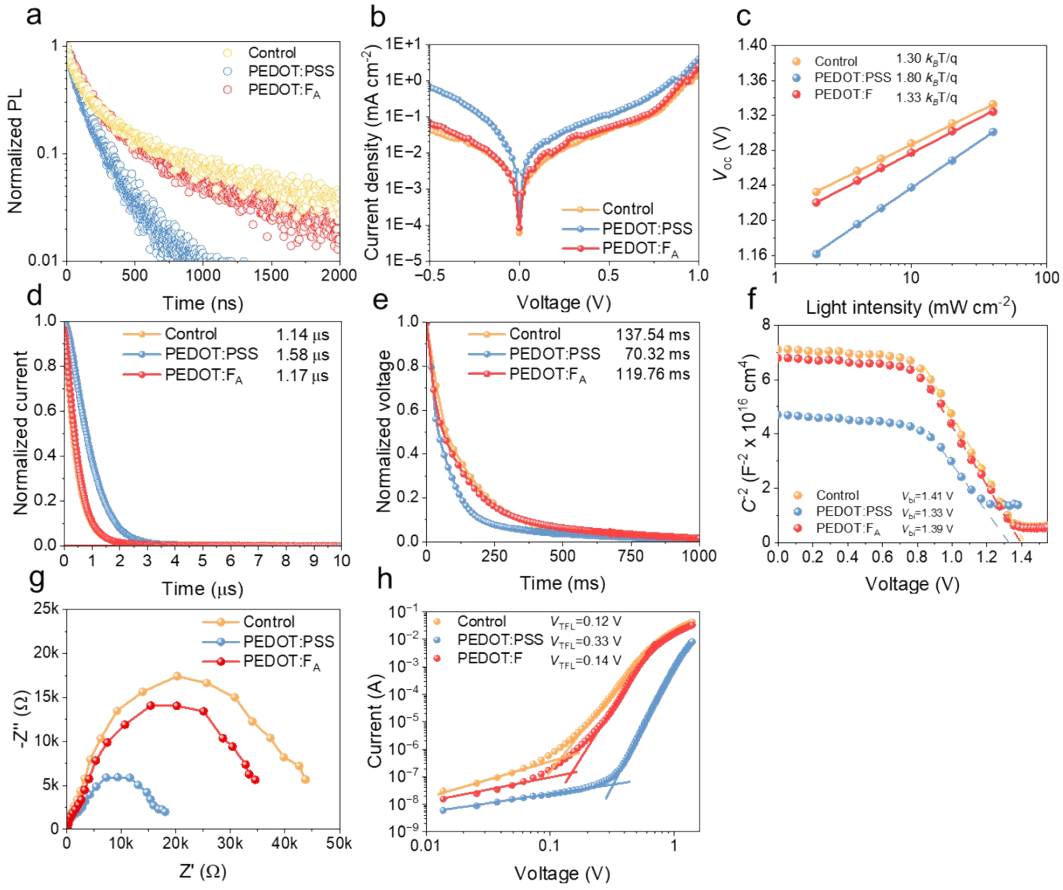

Fig. S25. (a) Time-resolved PL decay curves for the control, PEDOT:PSS, PEDOT:F_A deposited and ICL removal perovskite films when excited from the perovskite side. (b) Dark *J-V* curves of the control, PEDOT:PSS and PEDOT:F_A reconstructed PSCs. (c) The correlation between V_{oc} and light intensity of the control, PEDOT:PSS and PEDOT:F_A reconstructed PSCs. (d) TPC measurements for the control, PEDOT:PSS and PEDOT:F_A reconstructed PSCs. The photocurrent decay time is 1.14 μs, 1.58 μs and 1.17 μs for the control, PEDOT:PSS and PEDOT:F_A reconstructed PSCs, respectively. (e) Transient photovoltage (TPV) measurements for the control, PEDOT:PSS and PEDOT:F_A reconstructed PSCs. The photovoltage decay time is 137.54 ms, 70.32 ms and 119.76 ms for the control, PEDOT:PSS and PEDOT:F_A reconstructed PSCs, respectively. (f) The Mott-Schottky measurements for the control, PEDOT:PSS and PEDOT:F_A reconstructed PSCs. (g) Electrochemical impedance spectroscopy (EIS) analysis of the control, PEDOT:PSS and PEDOT:F_A reconstructed PSCs. (h) *J-V* characteristics of electron-only devices for the control, PEDOT:PSS and PEDOT:F_A reconstructed devices by SCLC method. V_{TFL} (trap-filled-limit voltage) is determined to be 0.12 V, 0.33 V and 0.14 V for the control, PEDOT:PSS and PEDOT:F_A reconstructed devices, respectively.

Actually, the aqueous PEDOT:PSS deposition would damage the WBG perovskite sub-sells, causing unwanted WBG perovskite halide segregation. While using the PEDOT:FA HTL will preserve the WBG perovskite films, preventing the solvent erosion from the rear cell HTL fabrication.

a

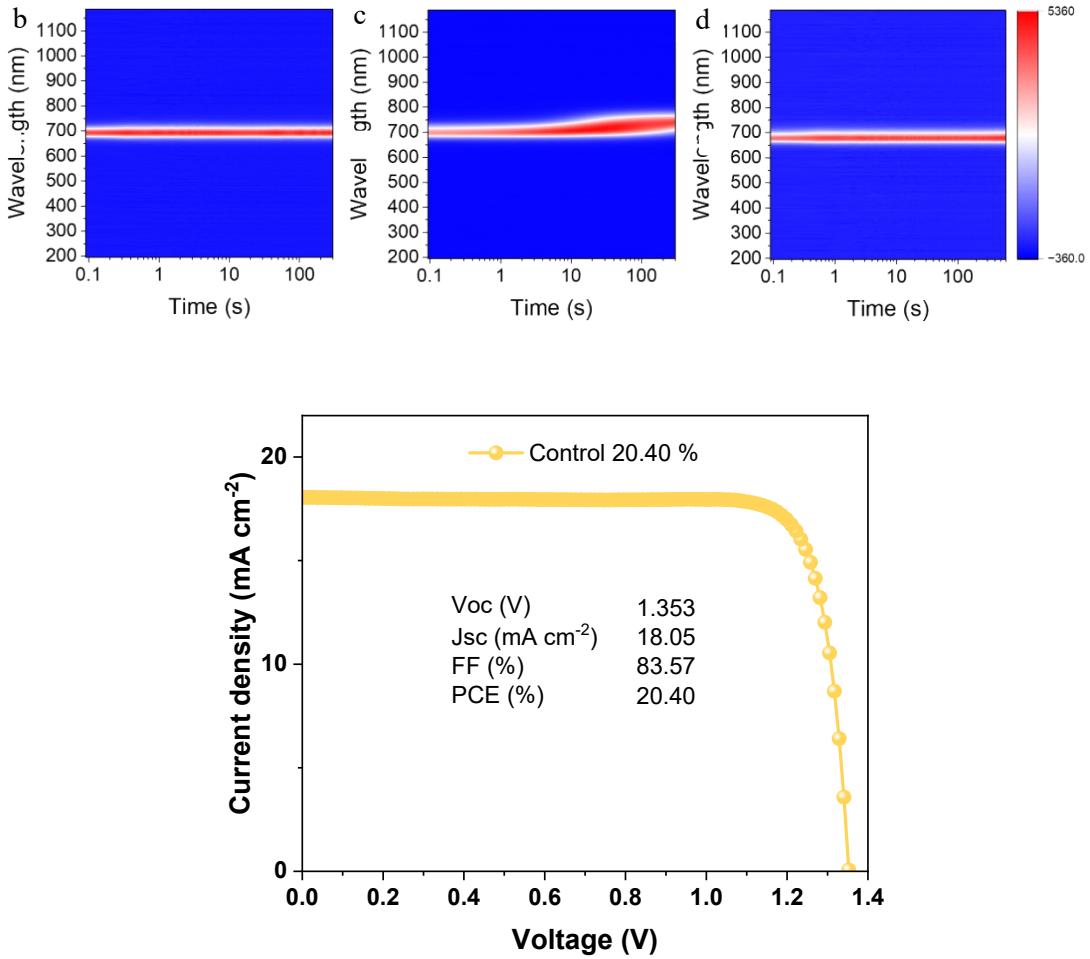

Fig. S26. (a) *J–V* curves of reconstructed control WBG PSC. In situ PL measurements with varying time of the control (b), PEODT:PSS (c) and PEDOT:F_A (d) based and ICL removed

WBG perovskite films.

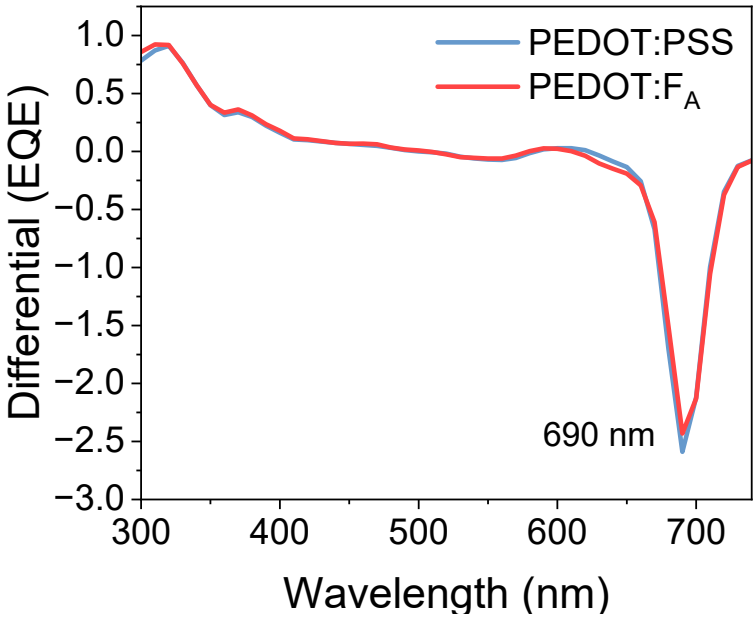

Fig. S27. The corresponding first derivatives of the EQE spectra from WBG perovskite solar cells for bandgap determination.

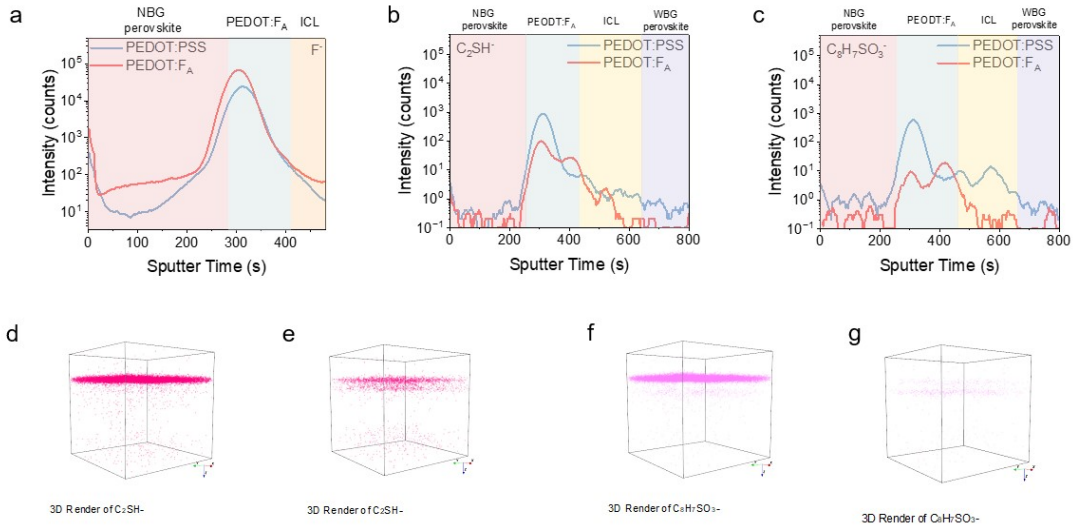

Fig. S28. ToF-SIMS F^- (a), C_2SH^- (b) and $C_8H_7SO_3^-$ (c) ions depth profile of PEDOT:PSS and PEDOT:F_A samples for the structure of Glass/SAM/WBG perovskite/C_{60}/ALD-SnO_2/Au/PEDOT/NBG perovskite. Reconstructed three-dimensional images of C_2SH^- ions distribution for the PEDOT:PSS (d) and PEDOT:F_A

(e) samples. Reconstructed three-dimensional images of $C_8H_7SO_3^-$ ions distribution for the PEDOT:PSS (f) and PEDOT:F_A (g) samples.

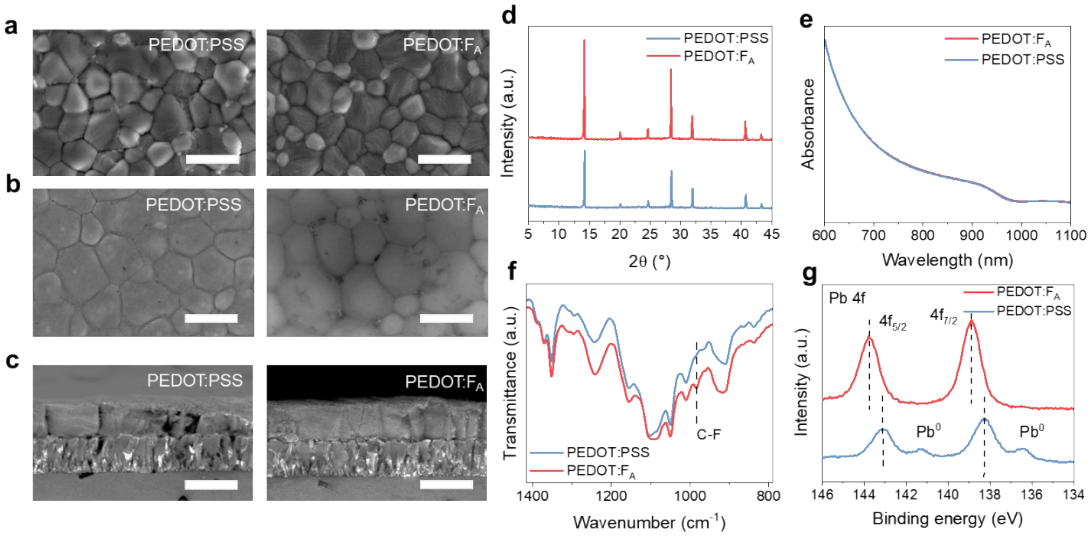

Fig. S29. Top (a), buried interface (b) and cross-sectional (c) SEM images of the NBG perovskite films fabricated on PEDOT:PSS and PEDOT:F_A-coated FTO glass substrates. Scale bars, 1 μm. (d) XRD of the NBG perovskite films fabricated on PEDOT:PSS and PEDOT:F_A-coated FTO glass substrates. (e) Ultraviolet-visible absorption spectra of the NBG perovskite films fabricated on PEDOT:PSS and PEDOT:F_A-coated FTO glass substrates. (f) FTIR peaks of buried interface NBG perovskite films peeling off form the PEDOT:PSS and PEDOT:F_A-coated FTO glass substrates. (g) XPS analysis of buried interface NBG perovskite films peeling off form the PEDOT:PSS and PEDOT:F_A-coated FTO glass substrates.

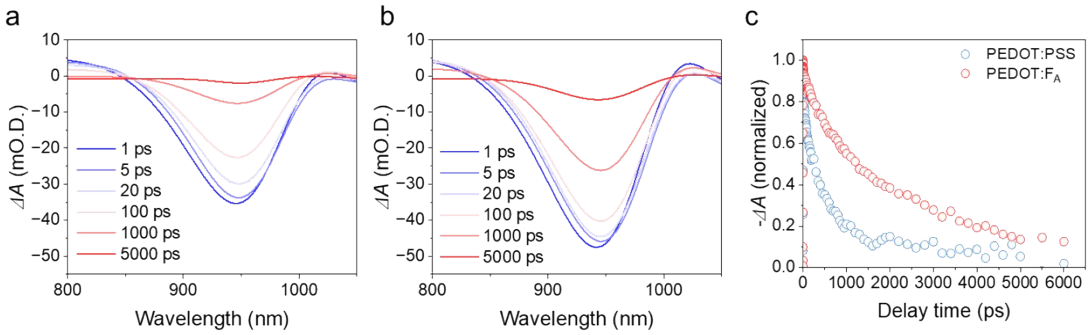

Fig. S30. Time-dependent transient fs-TA spectra of PEDOT:PSS (a) and PEDOT:F_A (b) based NBG perovskite films. (c) The corresponding transient absorption change (measured in optical density) over a timescale of 6000 ps.

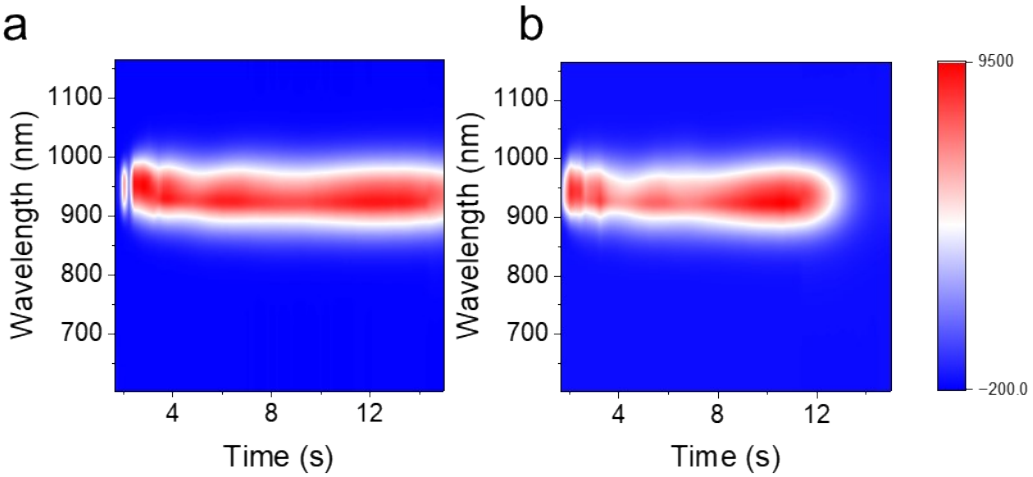

Fig. S31. In situ PL measurements maps of the NBG perovskite films on PEDOT:PSS (a) and PEDOT:F_A (b) HTL.

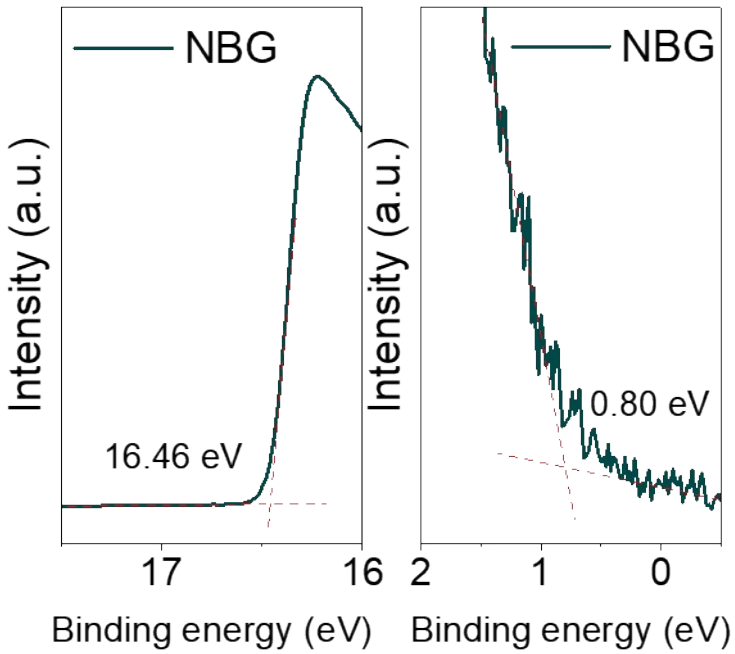

Fig. S32. UPS spectra of the control NBG perovskite films. The secondary electron cut-off (SECO) and the valence band maximum (VBM) are indicted.

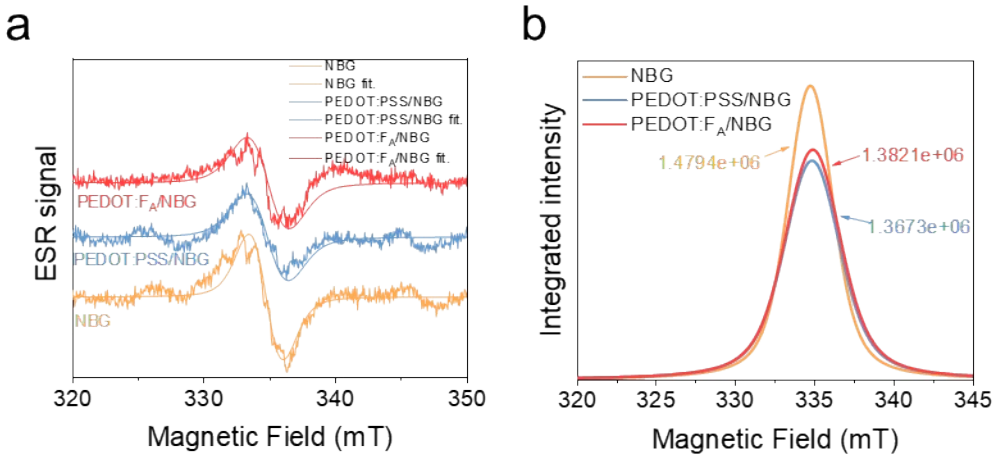

Fig. S33. The ESR spectra (a) and the integrated ESR spectra (b) for the NBG perovskite films on glass, with or without PEDOT:PSS and PEDOT:F_A HTL.

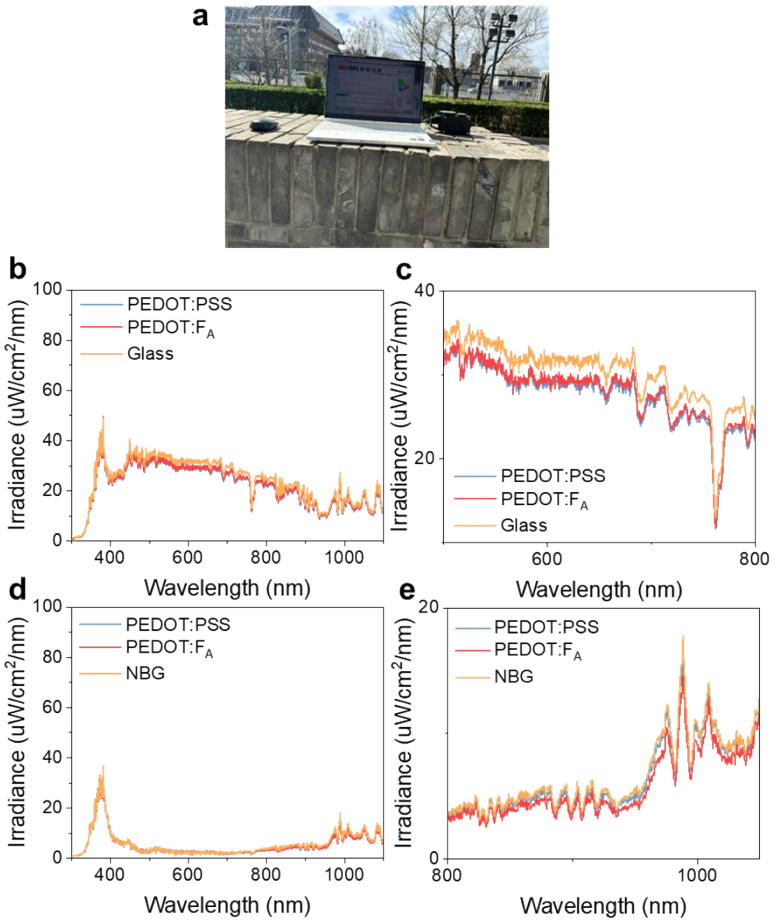

Fig. S34. (a) The local spectrum setup measured outdoor in the School of Physics, Peking University. Location: *39°59'26.00" N, 116°18'12.63" E*. The local spectrum (b) and zoom-in spectrum (c) filtered with glass, Glass/PEDOT:PSS and Glass/PEDOT:F_A. The local spectrum (d) and zoom-in spectrum (e) filtered with Glass/NBG perovskite, Glass/PEDOT:PSS/NBG perovskite and Glass/PEDOT:F_A/NBG perovskite.

The spectral irradiance was measured using a calibrated spectroradiometer (Ocean Optics), placed horizontally outdoors under direct sunlight. The probe was positioned behind each optical stack (e.g., glass, Glass/PEDOT:PSS, etc.), and the spectra were collected with consistent integration time and optical alignment under clear-sky conditions at local noon. The irradiance spectra are presented in relative intensity units due to lack of absolute calibration.

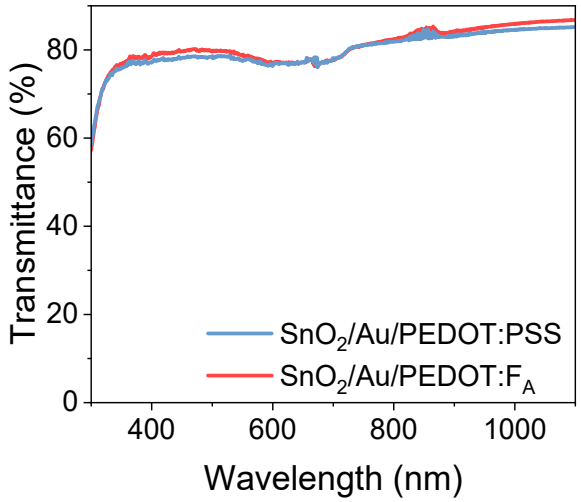

Fig. S35. The total transmittance spectra of ICLs (Glass/SnO_2/Au/PEDOT:PSS or Glass/SnO_2/Au/PEDOT:F_A). Slightly higher transmittance in the PEDOT:F_A configuration may be attributed to reduced parasitic absorption.

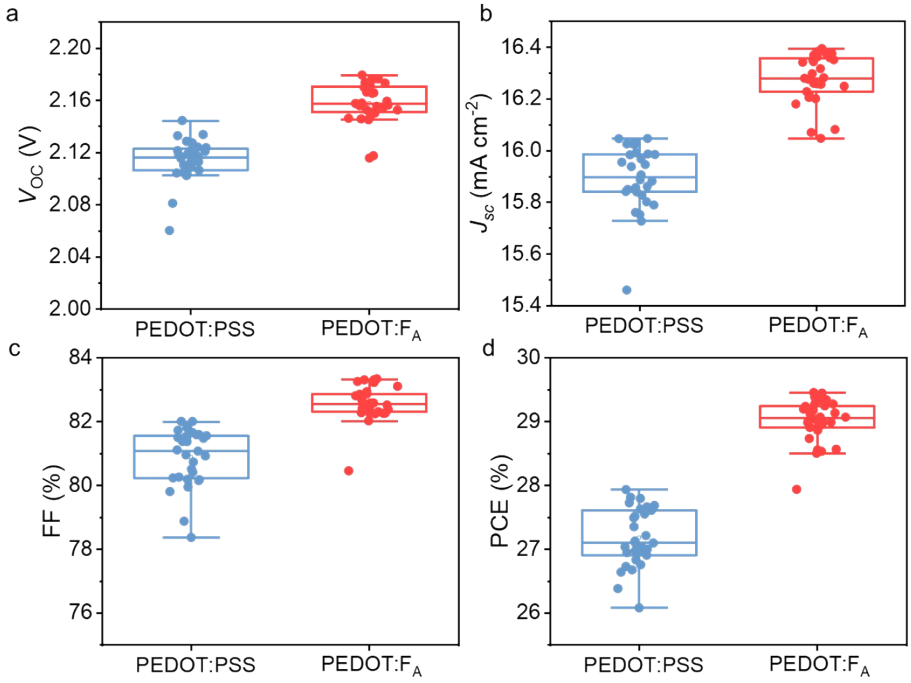

Fig. S36. Comparison of V_{oc} (a), J_{sc} (b), FF (c) and PCE (d) between PEDOT:PSS and PEDOT:F_A-based all-perovskite TSCs (30 devices for each type). The box lines indicate the standard deviation and the center represents the mean value.

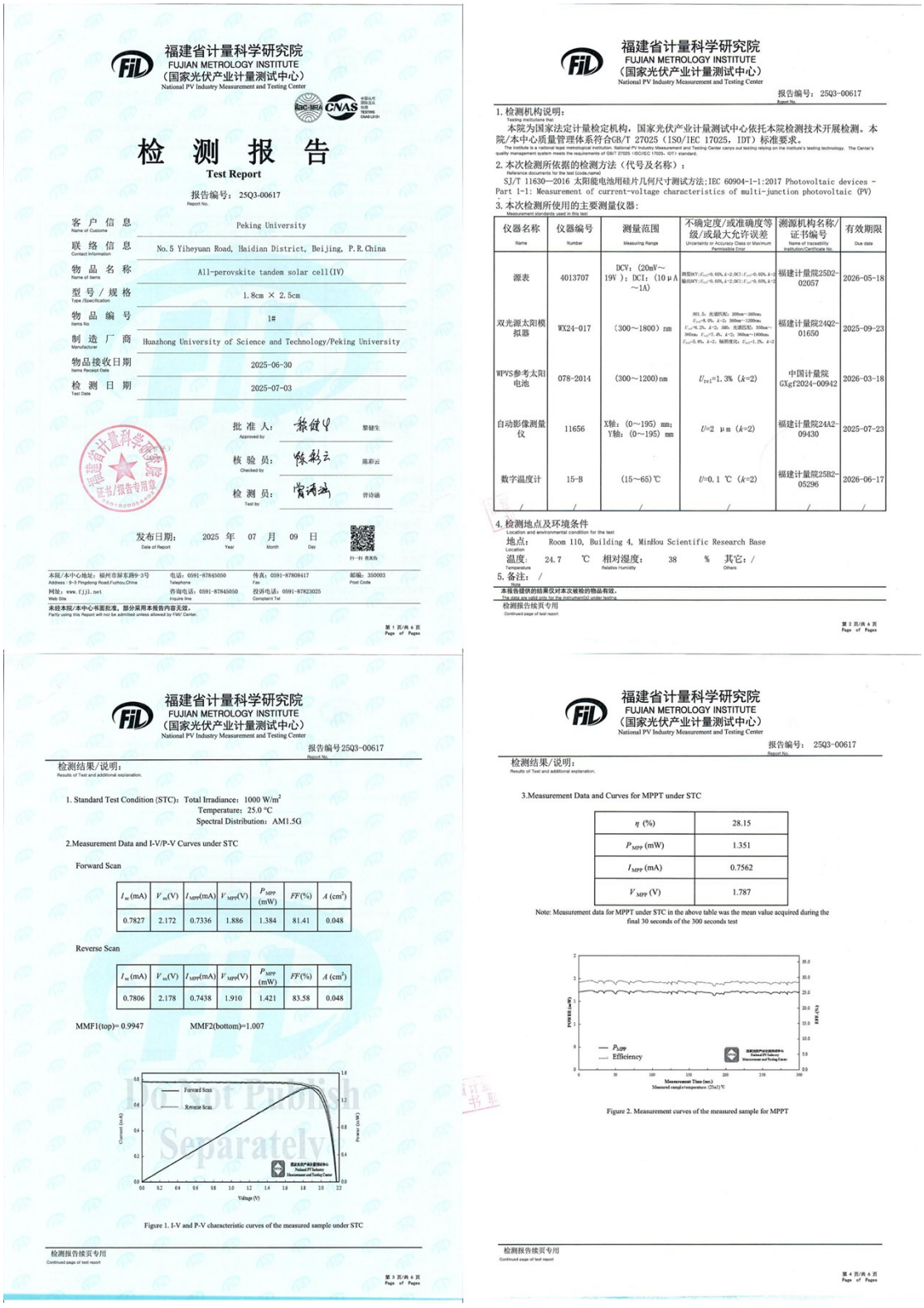

福建省计量科学研究院
FUJIAN METROLOGY INSTITUTE
（国家光伏产业计量测试中心）
National PV Industry Measurement and Testing Center

检 测 报 告
Test Report

报告编号：25Q3-00617

客户信息 Name of Customer	Peking University
联络信息 Contact Information	No. 5 Yiheyuan Road, Haidian District, Beijing, P. R. China
物品名称 Name of Items	All-perovskite tandem solar cell(IV)
型号/规格 Type /Specification	1.8cm × 2.5cm
物品编号 Items No.	1#
制造厂商 Manufacturer	Huazhong University of Science and Technology/Peking University
物品接收日期 Items Receipt Date	2025-06-30
检测日期 Test Date	2025-07-03

批准人：黎健甲 Approved by
核验员：陈彩云 Checked by
检测员：曾诗涵 Test by

发布日期：2025 年 07 月 09 日 Date of Report

本院/本中心地址：福州市屏东路9-3号 Address：9-3 Pingdong Road,Fuzhou,China
电话：0591-87845050 Telephone
传真：0591-87808417 Fax
邮编：350003 Post Code
网址：www.fjjl.net Web Site
咨询电话：0591-87845050 Inquire line
投诉电话：0591-87823025 Complaint Tel

未经本院/本中心书面批准，部分采用本报告内容无效。
Partly using this Report will not be admitted unless allowed by FMV Center.

第 1 页/共 6 页 Page of Pages

福建省计量科学研究院
FUJIAN METROLOGY INSTITUTE
（国家光伏产业计量测试中心）
National PV Industry Measurement and Testing Center

报告编号：25Q3-00617 Report No.

1. 检测机构说明：
Testing institutions that
本院为国家法定计量检定机构，国家光伏产业计量测试中心依托本院检测技术开展检测。本院/本中心质量管理体系符合GB/T 27025（ISO/IEC 17025，IDT）标准要求。
The Institute is a national legal metrological institution. National PV Industry Measurement and Testing Center carries out testing relying on the institute's testing technology. The Center's quality management system meets the requirements of GB/T 27025（ISO/IEC 17025，IDT）standard.

2. 本次检测所依据的检测方法（代号及名称）：
Reference documents for the test (code,name)
SJ/T 11630—2016 太阳能电池用硅片几何尺寸测试方法;IEC 60904-1-1:2017 Photovoltaic devices - Part 1-1: Measurement of current-voltage characteristics of multi-junction photovoltaic (PV)

3. 本次检测所使用的主要测量仪器：
Measurement standards used in this test

仪器名称 Name	仪器编号 Number	测量范围 Measuring Range	不确定度/或准确度等级/或最大允许误差 Uncertainty or Accuracy Class or Maximum Permissible Error	溯源机构名称/证书编号 Name of traceability institution/Certificate No.	有效期限 Due date
源表	4013707	DCV：(20mV～19V)；DCI：(10μA～1A)	按规范DCV：U_{rel}=0.03%, k=2;DCI：U_{rel}=0.03%, k=2 输出DCV：U_{rel}=0.03%, k=2;DCI：U_{rel}=0.03%, k=2	福建计量院25D2-02057	2026-05-18
双光源太阳模拟器	WX24-017	(300～1800) nm	对1.5s 光谱匹配：300nm～360nm U_{rel}=6.0%, k=2; 360nm～1200nm U_{rel}=2%, k=2; 1200nm～1800nm U_{rel}=6.0%, k=2; 对1.5s 光谱匹配：350nm～360nm U_{rel}=7.0%, k=2; 360nm～1800nm U_{rel}=5.0%, k=2; 辐照度比：U_{rel}=1.2%, k=2	福建计量院24Q2-01650	2025-09-23
WPVS参考太阳电池	078-2014	(300～1200) nm	U_{rel}=1.3% (k=2)	中国计量院 GXgf2024-00942	2026-03-18
自动影像测量仪	11656	X轴：(0～195) mm；Y轴：(0～195) mm	U=2 μm (k=2)	福建计量院24A2-09430	2025-07-23
数字温度计	15-B	(15～65) ℃	U=0.1 ℃ (k=2)	福建计量院25B2-05296	2026-06-17
/	/	/	/	/	/

4. 检测地点及环境条件
Location and environmental condition for the test
地点：Room 110, Building 4, MinHou Scientific Research Base Location
温度：24.7 ℃ Temperature 相对湿度：38 % Relative Humidity 其它：/ Others

5. 备注：/ Note

本报告提供的结果仅对本次被检的物品有效。
The data are valid only for the instrument(s) under testing.

检测报告续页专用
Continued page of test report

第 2 页/共 6 页 Page of Pages

福建省计量科学研究院
FUJIAN METROLOGY INSTITUTE
（国家光伏产业计量测试中心）
National PV Industry Measurement and Testing Center

报告编号25Q3-00617 Report No.

检测结果/说明：
Results of Test and additional explanation.

1. Standard Test Condition (STC)：Total Irradiance：1000 W/m^2
Temperature：25.0 ℃
Spectral Distribution：AM1.5G

2.Measurement Data and I-V/P-V Curves under STC

Forward Scan

I_{sc} (mA)	V_{oc}(V)	I_{MPP}(mA)	V_{MPP}(V)	P_{MPP} (mW)	FF(%)	A (cm^2)
0.7827	2.172	0.7336	1.886	1.384	81.41	0.048

Reverse Scan

I_{sc} (mA)	V_{oc}(V)	I_{MPP}(mA)	V_{MPP}(V)	P_{MPP} (mW)	FF(%)	A (cm^2)
0.7806	2.178	0.7438	1.910	1.421	83.58	0.048

MMF1(top)= 0.9947 MMF2(bottom)=1.007

Figure 1. I-V and P-V characteristic curves of the measured sample under STC

检测报告续页专用
Continued page of test report

第 3 页/共 6 页 Page of Pages

福建省计量科学研究院
FUJIAN METROLOGY INSTITUTE
（国家光伏产业计量测试中心）
National PV Industry Measurement and Testing Center

报告编号： 25Q3-00617 Report No.

检测结果/说明：
Results of Test and additional explanation.

3.Measurement Data and Curves for MPPT under STC

η (%)	28.15
P_{MPP} (mW)	1.351
I_{MPP} (mA)	0.7562
V_{MPP} (V)	1.787

Note: Measurement data for MPPT under STC in the above table was the mean value acquired during the final 30 seconds of the 300 seconds test

Figure 2. Measurement curves of the measured sample for MPPT

检测报告续页专用
Continued page of test report

第 4 页/共 6 页 Page of Pages

Fig. S37. Independent PCE certification report for PEDOT:F_A-based PSCs of a small area (0.048 cm^2) at Fujian Metrology Institute (National PV Industry Measurement and Testing Center). The certified PCE is 29.60% under reverse scan (J_{sc} of 16.26 mA cm^{-2}, V_{oc} of 2.178 V, and FF of 83.58%) and 28.83% under forward scan (J_{sc} of 16.31 mA cm^{-2}, V_{oc} of 2.172 V, and FF of 81.41%).

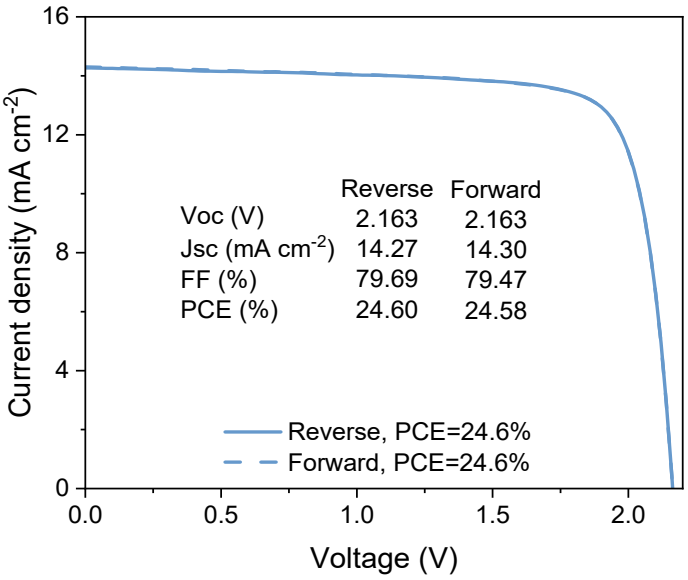

Fig. S38. *J-V* curves of the champion PEDOT:PSS-based perovskite/organic TSC with PM6:P2EH rear cell under 1-sun (100 mW cm^{-2}) illumination.

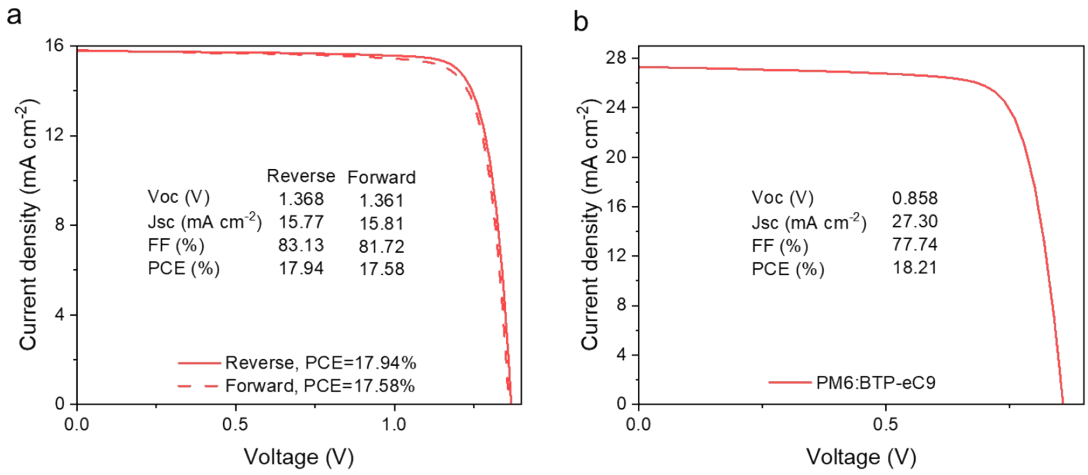

Fig. S39. *J-V* curves of the champion PEDOT:F_A-based WBG PSC (1.88 eV) (a) and PM6:BTP-eC9 organic solar cell (OSC) (b) under 1-sun (100 mW cm^{-2}) illumination.

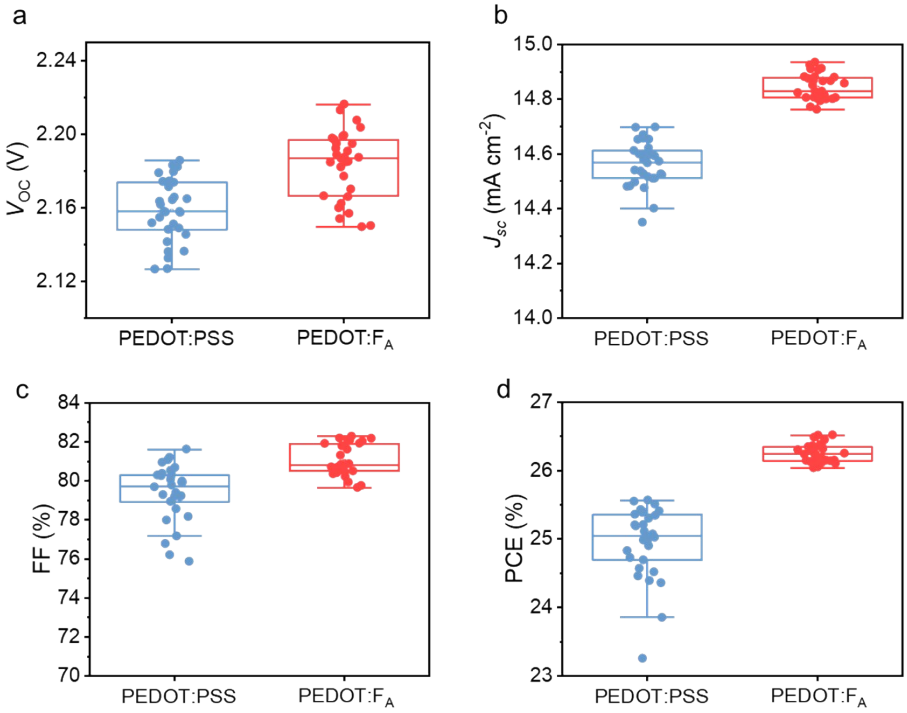

Fig. S40. Comparison of V_{oc} (a), J_{sc} (b), FF (c) and PCE (d) between PEDOT:PSS and PEDOT:F_A-based perovskite/organic TSCs (30 devices for each type). The box lines indicate the standard deviation and the center represents the mean value.

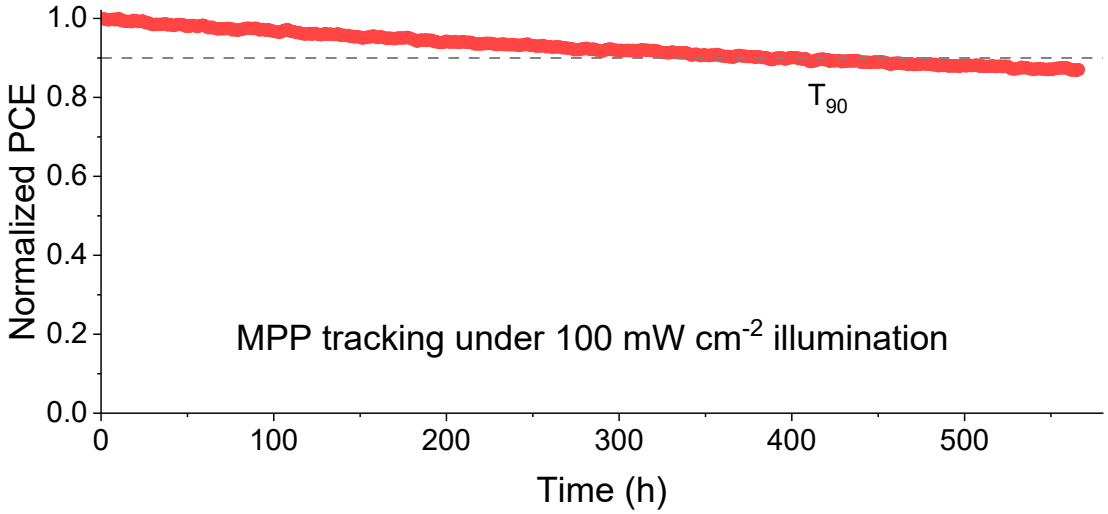

Fig. S41. Continuous MPP tracking of perovskite/organic TSCs for over 500 hours under simulated AM1.5 G illumination (100 mW cm^{-2}, LED simulator).

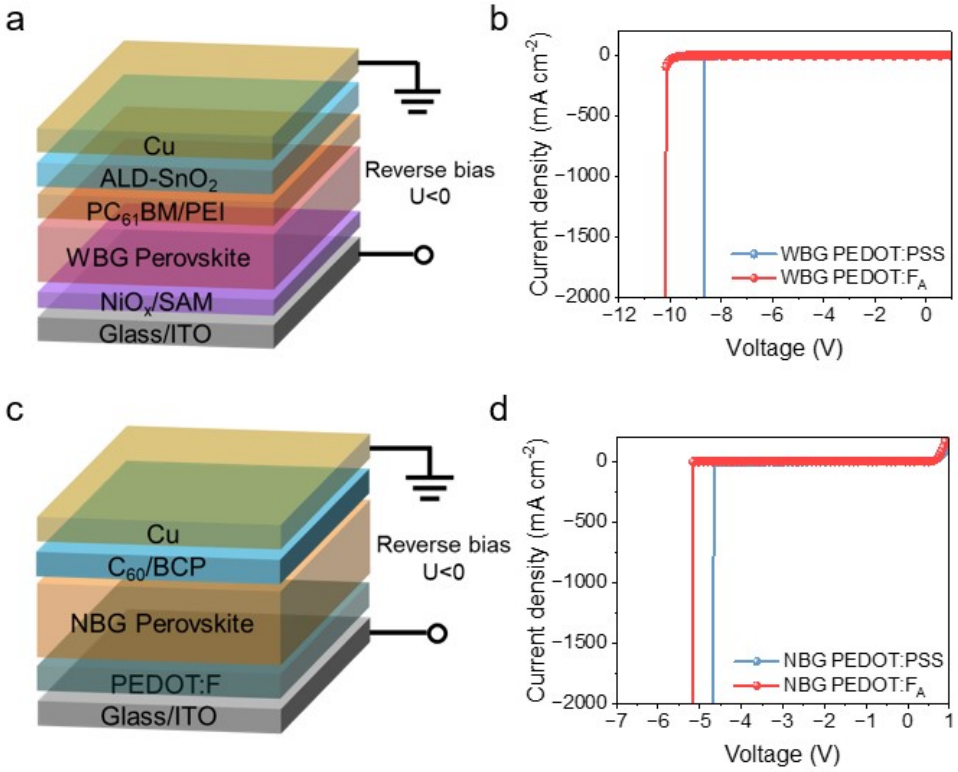

Fig. S42. Schematic diagram of the reconstructed WBG PSCs (a) and as NBG PSCs (c) (*U* represents the applied bias). The corresponding dark *J*-*V* curves of WBG PSCs (b) and NBG PSCs (d).

Table S1. Model parameters for tandem ICL photovoltaic architectures simulations.

Parameter	Value	Unit	Description
AuE	1×10^{-9}	m	Thickness of gold nano-islands
SnO_2E	2×10^{-8}	m	Thickness of SnO_2 layer
C_{60}E	2×10^{-8}	m	Thickness of C_{60} layer
AuD	2×10^{-9}	m	Spacing between Au islands
AuD0	2×10^{-9}	m	Diameter of individual Au islands
Dc	5×10^{-8}	m	Length of computational domain
AuN	25	—	Number of Au nano-islands (Dc/AuD0)
cw0	55,510	$mol \cdot m^{-3}$	Molar concentration of pure water
ϕSnO_2	0.01	—	Porosity of SnO_2
κSnO_2	5×10^{-20}	m^2	Permeability of SnO_2
ϕC_{60}	0.01	—	Porosity of C_{60}
κC_{60}	1×10^{-19}	m^2	Permeability of C_{60}
L_0	4×10^{-8}	m	Total porous layer thickness (SnO_2 + C_{60})
γ	0.0723	$N \cdot m^{-1}$	Surface tension of water
θ	54	degrees	Contact angle
Rc	8.8×10^{-7}	m	Capillary pore radius
pec	-1.36×10^5	Pa	Capillary entry pressure ($2\gamma \cdot \cos\theta/Rc$)
lp	2	—	Pore-size distribution index
ϕ	0.6	—	Overall porosity
K	5.81×10^{-14}	m^2	Hydraulic permeability ($\phi/8 \cdot Rc^2$)
ρair	1.0	$kg \cdot m^{-3}$	Density of air
ρwater	1.0×10^3	$kg \cdot m^{-3}$	Density of water
μair	1.76×10^{-5}	Pa·s	Dynamic viscosity of air
μwater	1.00×10^{-3}	Pa·s	Dynamic viscosity of water

Table S2. Composition and ratios derived from the high-resolution core-level scans.

	S (%)	C (%)	O (%)	F (%)
PEDOT:PSS	7.86	67.10	23.42	/
PEDOT:F_A	2.00	31.59	15.96	49.98

Table S3. Parameters of *J-V* curves of the best device based on PEDOT:PSS and PEDOT:F_A as HTL (small area).

	Scans	V_{oc} (V)	J_{sc} (mA cm^{-2})	FF (%)	PCE (%)
PEDOT:PSS	Reverse	0.857	32.51	80.47	22.42
	Forward	0.863	32.14	80.29	22.27
PEDOT:F_A	Reverse	0.865	32.84	81.68	23.21
	Forward	0.867	32.77	81.32	23.10

Table S4. Summary of photovoltaic parameters of champion WBG PSC, NBG PSC, and all-perovskite TSC.

	Scans	V_{oc} (V)	J_{sc} (mA cm^{-2})	FF (%)	PCE (%)
WBG PSC	Reverse	1.34	18.07	83.32	20.18
	Forward	1.34	18.01	82.13	19.84
NBG PSC	Reverse	0.88	32.93	80.16	23.13
	Forward	0.87	33.04	79.98	23.03
TSC	Reverse	2.18	16.42	83.26	29.73
	Forward	2.17	16.43	82.68	29.42

Table S5. Summary of photovoltaic parameters of champion WBG PSC, OSC, and perovskite/organic TSC.

	Scans	V_{oc} (V)	J_{sc} (mA cm^{-2})	FF (%)	PCE (%)
WBG PSC	Reverse	1.37	15.77	83.13	17.94
	Forward	1.36	15.81	81.72	17.58
NBG OSC	/	0.86	27.30	77.74	18.21
TSC	Reverse	2.19	14.80	81.91	26.52
	Forward	2.18	14.79	81.61	26.38

Table S6. Summary of the PCEs of all-perovskite TSCs published recently.

V_{oc} (V)	J_{sc} (mA cm^{-2})	FF (%)	PCE (%)	Reference
2.03	16.5	79.9	26.7 (26.4 certified)	***Nature*** 603, 73–78 (2022).
1.96	15.4	83.1	25.1 (24.6 certified)	***Nat. Energy*** 7, 744–753 (2022).
2.12	15.0	80.1	25.5 (24.3 certified)	***Nat. Energy*** 7, 642–651 (2022).
2.19	15.1	83.1	27.4 (26.3 certified)	***Nature*** 613, 676–681 (2023).
2.20	15.1	81.6	27.2	***Science*** 378, 1295–1300 (2022).
2.11	15.4	83.1	27.0 (26.4 certified)	***Nature*** 618, 80–86 (2023).
2.11	16.5	81.9	28.5 (28.0 certified)	***Nature*** 620, 994–1000 (2023).
2.11	16.0	82.2	27.8 (27.3 certified)	***Nature*** 624, 69–73 (2023).
2.13	15.5	82.4	27.2 (26.3 certified)	***Nat. Energy*** 8, 714–724 (2023).
2.11	15.9	81.4	27.3 (27.0 certified)	***Nat. Energy*** 9, 298–307 (2024).
2.17	16.4	83.3	29.7 (29.5 certified)	***Nat. Mate.*** 24, 252–259 (2025).
2.13	16.1	81.9	28.2	***Nat. Photon*** 19, 170–177 (2025).
2.17	16.3	83.3	29.6 (29.5 certified)	***Nat. Commun*** 16, 4917 (2025).
2.13	16.1	84.5	29.0 (28.9 certified)	***Nat. Photon*** 19, 426–433 (2025).
2.21	16.6	83.4	30.6 (30.1 certified)	**https://doi.org/10.1038/s41586-025-09773-7**
2.18	16.4	83.2	29.7 (29.6 certified)	**This work**

Table S7. Summary of the PCEs of perovskite/organic tandem solar cells published recently.

V_{oc} (V)	J_{sc} (mA cm^{-2})	FF (%)	PCE (%)	Reference
2.06	14.8	77.2	23.6	***Nat. Energy*** 7, 229-237 (2022).
2.15	14.0	80.0	24.0	***Nature*** 604, 280-286 (2022).
2.15	14.4	81.7	25.2	***Nat. Energy*** 9, 411-421 (2024).
2.12	14.7	83.0	25.8	***Nat. Energy*** 9, 592-601 (2024).
2.16	15.4	79.4	26.4	***Nature*** 635, 860–866 (2024).
2.14	15.4	83.7	27.5	***Nature*** 643, 104–110 (2025).
2.19	14.8	81.9	26.5	**This work**

References

1. Katahara, J. K. & Hillhouse, H. W, *Journal of Applied Physics*, 2014, 116 (17), 173504.

2. Braly, I. L., Stoddard, R. J., Rajagopal, A., Jen, A. K. Y. & Hillhouse, H. W, *The Journal of Physical Chemistry Letters*, 2018, *9* (13), 3779-3792.

3. COMSOL Multiphysics® v. 6.2. www.comsol.com. COMSOL AB, Stockholm, Sweden.

4. Cussler, E. L. (2009). Diffusion: Mass Transfer in Fluid Systems. Cambridge University Press.

5. Zimmerman, R. W. (2018). Fluid Flow in Porous Media. World Scientific.

6. Dullien, F. A. L. (2012). Porous Media: Fluid Transport and Pore Structure. Academic Press.

7. Kawagoe, Y., Oshima, T., Tomarikawa, K., Tokumasu, T., Koido, T., Yonemura, S., Microfluid Nanofluid, 2016, 20, 162.

8. Y. Jiang, X. Dong, L. Sun, T. Liu, F. Qin, C. Xie, P. Jiang, L. Hu, X. Lu, X. Zhou, W. Meng, N. Li, C. J. Brabec and Y. Zhou, Nature Energy, 2022, 7, 352–359.